UNIVERSITÀ DEGLI STUDI DI PADOVA

SCUOLA DI SCIENZE

DIPARTIMENTO DI FISICA E ASTRONOMIA

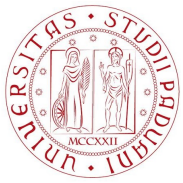

CORSO DI LAUREA MAGISTRALE IN ASTRONOMIA

Star formation properties of galaxies in a deep HST spectral imaging survey

Relatore: Dott.ssa GIULIA RODIGHIERO

Correlatore: Prof. ALBERTO FRANCESCHINI

Laureanda: ANNAGRAZIA PUGLISI

Anno accademico 2013/2014

Contents

Introduction

One of the most complex and less clarified arguments of the modern cosmology is the formation and evolution of galaxies, which trace the large scale structures of the Universe and can be used to evaluate its evolutive properties. To interpret the origin and the development of these systems during the cosmic time in a consistent way it is necessary a simultaneous study of all their components (stars, gas, dust and dark matter), possible only through an analysis of data in a broad range of wavelength. The multi-wavelength imaging surveys and the spectroscopical measurements have recently supplied a huge library of data on wide samples of galaxies from the local to the high redshift Universe. These data will allow to study the emission properties of several galaxy populations and to empirically reconstruct the global history of star formation and heavy elements production of the Universe.
The study of star formation processes that take place in a galaxy and their evolution with cosmic time is a key element to understand galaxy formation. One of the most important quantities in the characterization of a galaxy is the rate at which it converts gas into stars, the Star Formation Rate (SFR). The star formation rate can be quantified with several methods, depending on the observed wavelength (spectroscopic or photometric) of the available data for a given sample, therefore it is fundamental to determine the correlation between various SFR estimators to compare different measurements.
The presence of dust has a great impact on the interpretation of multi-wavelength data, expecially at high redshift. Dust grains, in fact, absorb the flux emitted by stars at ultraviolet and optical wavelengths and re-emit it at larger wavelength, in the infrared bands. Star forming regions are dusty environments and the youngest stars, that trace the episodes of recent stellar formation, have the peak of the emission in the UV-optical parts of the spectrum hence their energy output results strongly attenuated by dust. Quantifying with accuracy the impact of dust on the integrated emission of a galaxy is extremely important to precisely evaluate the star formation rate. Many dust extinction corrections have

been elaborated across the years, both from theoretical models and from empirical calibrations.

The main purpose of this work is to evaluate the SFR from different star formation indicators and to determine the best correction for dust extinction on a sample of star forming galaxies at high redshift ($z \in [0.7-1.5]$). The sample is composed by 87 sources detected at far-infrared wavelengths by the Herschel Space Telescope (from the PEP survey) with a strong Hα emission in the GOODS-Southern field. The sources have near infrared spectra, acquired through the slitless survey 3D-HST, from which we can compute Hα flux measurements and a spectroscopic estimate of redshift. The HST data are compared with ancillary photometric data in order to build up the Spectral Energy Distribution (*SED*) for all the objects in the sample.
We compute for the sample a measure of the SFR from the infrared+ultraviolet luminosity and from the Hα luminosity. We apply several dust extinction correction to the Hα luminosities, following the approach of various authors. We determine the best extinction factor for our sample by comparing the SFR indicators considered in this Thesis.

In the 1^{st} chapter we describe the principal methods to estimate the Star Formation Rate. The 2^{nd} chapter contains the description of PEP and 3D-HST surveys. In the 3^{rd} chapter we describe the sample selection. The 4^{th} chapter describes the spectral analysis: we report the calibration of the 3D-HST team, the computation of Hα fluxes, the spectroscopic redshifts estimate and the evaluation of the aperture corrections from two different methods. The 5^{th} chapter illustrates the procedure of SED fitting. The 6^{th} chapter describes the methods used to correct the Hα fluxes for dust extinction. In the 7^{th} chapter we show the measurements of Star Formation Rates and the comparison between SFR indicators. Finally, the 8^{th} chapter presents the conclusions.

Chapter 1

The Star Formation Rate

An essential measurement to infer the evolutionary state of a galaxy is the rate at which this converts its gaseous mass in stars, that is the Star Formation Rate (SFR).
There are several ways to quantify the star formation rate. The most diffuse methods come from measurements in the UltraViolet (UV) part of the spectrum, from fluxes of nebular recombination lines (e.g. Hα) or from the far-InfraRed (far-IR) emission. UV wavelengths trace recent star formation processes because the luminosity in these bands is related to the youngest stars. However, star formation takes place in dusty environments so L_{UV} is strongly absorbed and it is not a valid tracer of SFR, in absence of correction for dust extinction. The absorbed radiation is thermally emitted in the infrared part of the spectrum, so the galaxy luminosity at these wavelengths represents a complementary SFR indicators. The youngest stars ionize the surrounding medium, producing recombination lines that allow us to constrain again the SFR of a galaxy. Also in this case the effects of dust extinction are not negligible.
The extinction by dust is one of the principal uncertainty since it is a dominant component of the star forming regions. Understanding the impact of dust on spectra of star forming galaxies is fundamental to constrain the star formation events in the Universe.

In this chapter we briefly discuss the SFR indicators adopted in this Thesis. Most of the discussion is based on the rewiew work of Kennicutt (1998) [20].

1.1 Star Formation Rate from UltraViolet continuum

The integrated spectrum of a galaxy in the wavelength range between $\lambda \in [1250 - 2500]$Å is dominated by the emission of young stars and the SFR scales linearly with luminosity.
The conversion between the UV flux over a given wavelength interval and the SFR can be derived using synthesis models. The calibration of Madau et al. (1998) [31] with a Salpeter (1955) [41] Initial Mass Function (IMF) and mass limits between 0.1 and 100 $M_\odot$ yields:

$$SFR_{UV}[M_\odot/yr] = 1.4 \times 10^{-28} L_{UV}[erg/s/Hz] \tag{1.1}$$

where L_{UV} is the luminosity in the wavelength range $\lambda \in [1500 - 2800]$ Å.
This technique is directly tied to the photospheric emission of the young stellar population and it can be applied to star forming galaxies over a wide range of redshifts.
The drawbacks of the method are its sensitivity to the form of the IMF, to the metallicity of the stellar populations and to the extinction by dust. The obscuring effect of dust is the main uncertainty in the determination of SFR from UV light because the effects of dust extinction are stronger in this part of the spectrum. A reliable measurement of star formation rates from UV light must either correct for the effects of dust absorption, or measure the absorbed energy directly through infrared emission.

1.2 Star Formation Rate from far-InfraRed continuum

A significant fraction of the bolometric luminosity of a galaxy is absorbed by the interstellar dust and is re-emitted in the thermal IR at wavelengths of roughly $\lambda \in [10 - 300]\mu$m.
The absorption cross section of the dust is strongly peaked in the ultraviolet and since most of the UV emission comes from star formation, the infrared luminosity is interpreted to be a sensitive tracer of the star formation rate of a galaxy.
The efficacy of the far-IR luminosity as a SFR tracer depends on the contribution of young stars to the heating of dust and on the optical depth of the dust in the star forming regions. The simplest physical situation is one in which young stars dominate the radiation field throughout the UV-visible, and the dust opacity is high everywhere, in which case the far-IR

luminosity measures the bolometric luminosity of the starburst. In such a limiting case the far-IR luminosity is the best SFR tracer, providing what is essentially a calorimetric measure of the SFR. Such conditions roughly hold in the dense circumnuclear starbursts that power many IR-luminous galaxies.
The physical situation is more complex in the disks of normal galaxies where the far-IR spectra contain both a "warm" component related to the dust around young star forming regions ($\lambda \sim 60\mu m$), and a cooler "infrared cirrus" component ($\lambda \geq 100\mu m$) which is associated with more extended dust heated by the interstellar radiation field.
The SFR vs L_{IR} conversion is derived using synthesis models. In the optically thick limit, it is only necessary to model the bolometric luminosity of the stellar population. The major uncertainty in this case is the adoption of an appropriate age for the stellar population. Applying the models of Leitherer & Heckman (1995) [27] for continuous bursts of age 10-100 Myr, and adopting the Salpeter IMF, yields the relation (Kennicutt (1998) [21]):

$$SFR_{IR}[M_{\odot}/yr] = 1.7 \times 10^{-10} L_{IR}[L_{\odot}] \tag{1.2}$$

where L_{IR} refers to the infrared luminosity integrated over the full mid and far-IR spectrum (8-1000 μm). Here, it is assumed that the infrared emission is entirely due to recent star formation but the presence of an Active Galactic Nucleus (AGN) or an older stellar population can also contribute to dust heating. If also the net dust opacity to young star-forming regions in a galaxy is not large, the star formation rate derived from the infrared luminosity will only represent a fraction of the total. The conversion factor between L_{IR} and SFR_{IR} will also depend on the details of the star formation history and on metallicity. The far-IR luminosities share also the same IMF dependence as the other direct star formation tracers.

1.3 Star Formation Rate from recombination lines

The nebular lines re-emit the integrated stellar luminosity of galaxies shortward of the Lyman limit, so they provide a direct, sensitive probe of the young massive stellar populations. Most applications of the estimate of SFR from recombination lines have been based on measurements

of the Hα line flux, but other recombination lines including Hβ, Pα, Pβ, Brα, and Brγ have been used as well. Other lines from heavier elements have also been used, but tend to have more complex dependence on the InterStellar Medium (*ISM*) conditions such as metallicity or excitation. The conversion factor between ionizing flux and the SFR is usually computed using an evolutionary synthesis model. Only stars with masses larger than 10 $M_{\odot}$ and lifetimes lower than 20 Myr contribute significantly to the integrated ionizing flux, so the emission lines provide a nearly instantaneous measure of the SFR, independent from the previous star formation history. For solar abundances and Salpeter IMF, the calibrations of Kennicutt et al. (1994) [23] and Madau et al. (1998) [31] yield:

$$SFR[M_{\odot}/yr] = 7.9 \times 10^{-42} L_{H\alpha}[erg/s] \tag{1.3}$$

The Hα calibration is computed for Case B recombination at $T_e = 10000$ K, then for an optically thick nebula where recombinations to the ground state generate photons that are absorbed locally ("on the spot" approximation).
The primary advantages of this method are its high sensitivity and the direct coupling between the nebular emission and the massive SFR, since Hα emission arises primarily from HII regions photoionized by O stars with lifetimes shorter than 20 Myr, although the presence of AGN can also contribute to these lines. The most important source of systematic error in Hα-derived SFRs is the extinction. The other chief limitations of the method are its sensitivity to the form of the IMF and the [NII] contamination to the Hα emission, in particular for low resolution spectra.

In this Thesis we obtain an estimate of the star formation rate on a sample of star forming galaxies at redshift z $\in [0.7 - 1.5]$, from the Hα fluxes derived from slitless spectra.
The Hα fluxes are corrected for dust extinction with different methods, presented in the 6^{th} chapter . We hence compute various estimates of the SFR from the Hα line luminosities by varying the correction for dust extinction.
We calculate an independent estimate of the SFR starting from the sum of UV luminosity, derived from the monochromatic luminosity at 2007 Å, and total IR luminosity, derived from the SED fitting (see the 5^{th} chapter for details about the computation of the SEDs). We assume that this is our best estimate of SFR and we compare SFR_{IR+UV} and $SFR_{H\alpha}$ by varying the correction for dust extinction. If we assume that SFR_{IR+UV}

and $SFR_{H\alpha}$ are intrinsically the same quantity, the scatter in the plots is due to the dust extinction so we can evaluate the best procedure to correct for the extinction.

Chapter 2

Extragalactic multi-wavelength surveys

2.1 The Herschel Space Observatory

Herschel [1] is a pioneering mission of the scientific program of ESA and observes the far-IR the sub-mm parts of the spectrum .
The telescope was succesfully launched on 14^{th} May 2009 and it was working autonomously in an elliptic orbit arount the second lagrangian point L2 of the orbital system Sun-Hearth-Moon. Figure 2.1 shows the Herschel Space Telescope and its orbit.

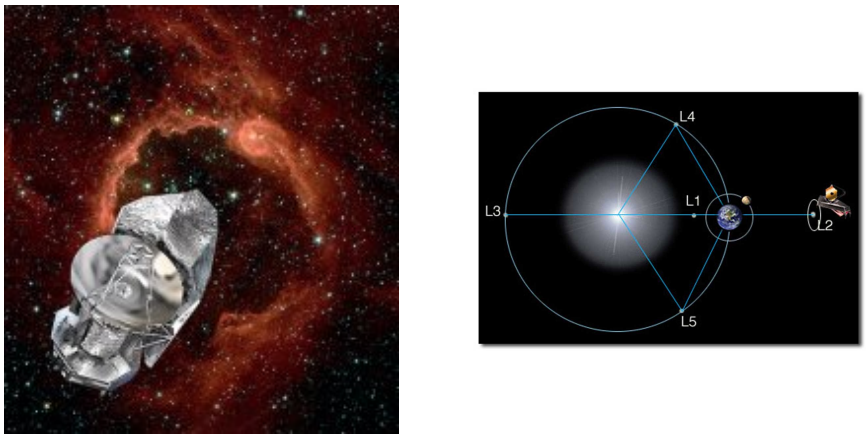

Figure 2.1: The Herschel Space Observatory and its orbit.

The instrument style is a classic *Cassegrain* telescope. Herschel was equipped with a primary mirror of 3.5m of diameter, cooled by liquid

[1] `http://herschel.esac.esa.int/`

helium. The scientific instrumentation is composed by three instruments:

- *PACS* (Photodetector Array Camera and Spectrometer, Poglitsch and Altieri (2009) [36]) can operate as a camera and as a spectrograph in a wavelength range $\lambda \in [55 - 210]\mu$m;
- *SPIRE* (Spectral and Photometric Imaging REceiver, Griffin et al. (2009) [16]) is complementary to the previous and observes between 194 and 672 μm;
- *HIFI* (Heterodyne Instrument for the Far Infrared, de Graauw et al. (2009) [10]) is an high resolution spectrometer and covers the bands $157 - 212$ μm and $240 - 625$ μm, using a mix of superconductors as detector.

The three devices allow to perform *imaging* and spectroscopy in a wide spectral range. Figure 2.2 shows the focal plane of Herschel and the transmission curve of PACS.

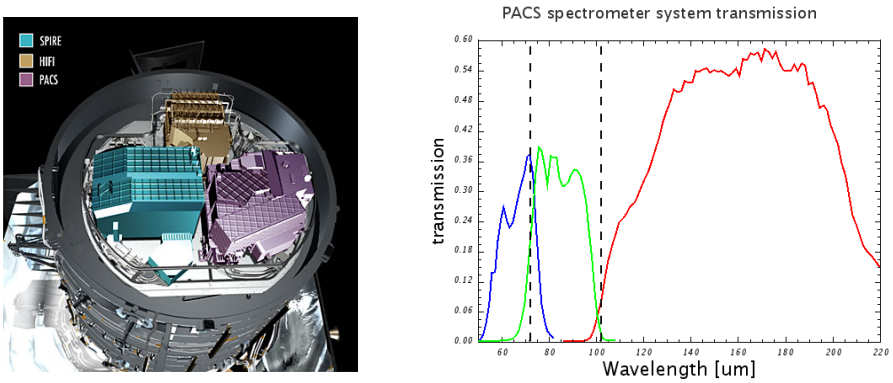

Figure 2.2: *Left:* Focal plane of the Herschel space telescope. From `http://starformation-herschel.iap.fr/herschel-outreach`
Right: Throughput curve of the PACS instrument. From `http://herschel.esac.esa.int/Docs/PACS/html/ch04s03.html`

2.1.1 The Herschel *PEP* survey

The ESA's Herschel space observatory (Pilbratt (2010) [35]) and its PACS and SPIRE instruments allowed observations in the far-IR and sub-mm. The PACS Evolutionary Probe (*PEP*) is a deep extra-galactic survey of guaranteed time (P.I. D.Lutz), centered on the observations of the PACS instrument at 70, 100 and 160 μm. The project intends to study the cosmic evolution of dust and of the infrared luminosity function, highlighting the relationship between environment and far-IR emission. The other important goal is the computation of the infrared emission and the study of energy processes which occur in the galaxy population at high redshift (Lutz et al. (2011) [29]).
The deepest field analyzed by the PEP survey is the Great Observatories Origins Deep Survey (*GOODS*); in particular the GOODS-South field is the only one observed also at 70 μm. Figure 2.3 shows the GOODS-Southern field as observed by PACS.

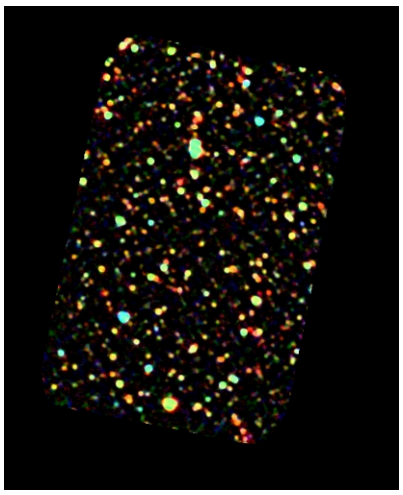

Figure 2.3: Herschel/PACS picture of the GOODS-South at wavelengths of λ 70, 100 and 160 μm.
This false colors picture was realized by mapping the 70μm in blue, the 100μm in green and the 160μm in red.
Fom `http://sci.esa.int/science-e/www/object/index.cfm?fobjectid=49192`

R.A.:	53.12654°
Dec:	-27.80467°
Dimension:	17×11 *arcmin*
λ:	70, 100, 160 μm

Catalog and PEP-Herschel photometry

PACS's catalogs are extracted from the corresponding maps at 70, 100 and 160 μm, following two methods optimized for the different goals of the PEP project. The PEP team provided a "blind" extraction (Diolaiti et al. (2000)[11], Berta et. al (2010)[1]) and a guided extraction with "priors", using mainly sources' positions detected at 24 μm. The two methods leads to similar results (Magnelli et al. (2009) [32]). The extracted fluxes are consistent to each other and allow to build up a deep catalog.
To quantify the reliability of the extracted fluxes, the incompleteness level and the fraction of spurious sources, Monte Carlo simulations were realized creating 500 images and adding 20 artificial objects on each map. The input and output fluxes are consistent. The completeness is defined as the source fraction detected with a photometric accuracy of about 50%. Spurious sources are defined as the sources extracted above 3σ with an input flux lower than 3σ.
In the GOODS-S field the 3σ limit is respectively of 1.0 mJy, 1.2 mJy and 2.4 mJy at 70,100 and 160 μm.

The sample adopted in this Thesis is selected starting from PEP sources in the GOODS-Southern field. The photometric Herschel's data are correlated with the spectroscopic observations in the 3D-HST survey with a cross-correlation between sources positions in R.A. and Dec. The cross-correlation was realized with the multi-wavelength catalog GOODS-MUSIC. For details about the catalog and the procedure of sample selection we refer to the 3^{rd} chapter.

2.2 The Hubble Space Telescope

The Hubble Space Telescope[2] (*HST*) is a common project of space agencies NASA and ESA and was launched in orbit on 24^{th} April 1990. Figure 2.4 shows the Space Telescope and its orbit.

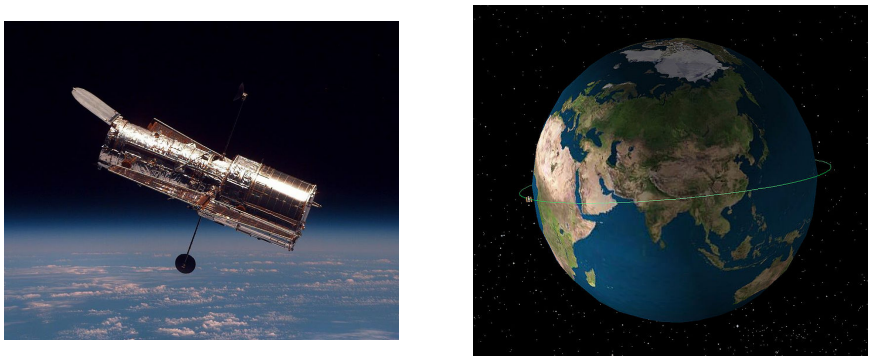

Figure 2.4: The Hubble Space Telescope and its orbit.

HST is a *Cassegrain* styled reflector, provided with a primary parabolic mirror with a diameter of 2.4 m, and covers observations in the spectral regions of UV, optical and near-IR.
The telescope orbits around the Hearth at an altitude of 569 km and was projected to be reached by astronauts. During the years, HST was equipped with a lot of instruments and provided an enormous amount of data for all the research fields in Astronomy.

2.2.1 The 3D-HST survey

The 3D-HST[3] (Brammer et al. (2012)[3], Skelton et al. (2014) [45]) near-infrared survey was designed to provide spectroscopical information for a huge number of objects in the observed fields, in order to study the physical processes that shape galaxies in the far Universe.
This Treasury program has been allocated 248 primary+parallel orbits of HST time over Cycles 18 and 19 to surveying $\sim 600\ arcmin^2$ of well studied extragalactic survey fields with two orbits of primary WFC3/G141 grism coverage and two to four orbits with ACS/G800L coverage.
3D-HST covers roughly 75% of the area imaged by the CANDELS survey (Grogin et al. 2011[17], Koekemoer et al. 2011[24]). The observed fields are the best-studied extragalactic survey fields and offer a wealth

[2] `http://www.stsci.edu/hst`
[3] `http://3dHST.research.yale.edu`

of deep, multi-wavelength imaging and spectroscopic observations from large number of previous ground-based and space-based surveys. Table 2.1 summarizes the position of each observed field, the number of pointings and the HST's instruments used to acquire the data.

Field	**R.A**	**Dec.**	**N pointings**	**Regions**
AEGIS	14:19:31	+52:51:00	30	WFC3 / ACS
COSMOS	10:00:29	+02:20:36	28	WFC3 / ACS
GOODS-S	***03:32:31***	***-27:48:54***	***34***	***WFC3***/ACS
HUDF09	03:32:39	-27:47:01	4	WFC3
UKIDSS-UDS	02:17:26	-05:12:13	28	WFC3 / ACS
GOODS-N	12:36:50	+62:14:07	28	WFC3

Table 2.1: The fields observed in the 3D-HST survey.

In the following paragraphs we present a brief summary about the instrumentations used by the 3D-HST survey. The primary observations were done with the WFC3/G141 grism for the spectroscopy mode and with the F140W filter for the imaging mode. In addition to the primary WFC3 observations, 3D-HST obtained parallel ACS F814W imaging and G800L grism spectroscopy.

The G141 grism

The WFC3 G141 grism is the primary spectral element used for the survey. The combined transmission of the telescope assembly and the primary spectral order of the G141 grism is larger than 30% in a wavelength range from 1.1 to 1.65 μm, reaching a peak of nearly 50% at a wavelength of 1.45 μm, as shown in figure 2.5. The mean dispersion of this order is 46.5 Å/px that corresponds to a resolution power of about $R \sim 130$, and varies by a few percent across the field of view. The uncertainties of the wavelength zero-point and dispersion of the G141 grism are 8 Å and 0.06 Å/px respectively.

Spectral features covered by this grism include Hα at $0.7 < z < 1.5$, $[OIII]_{\lambda 5007}$ at $1.2 < z < 2.3$, $[OII]_{\lambda 3727}$ at $2.0 < z < 3.4$ and the Balmer/4000Å break at $1.8 < z < 3.1$.

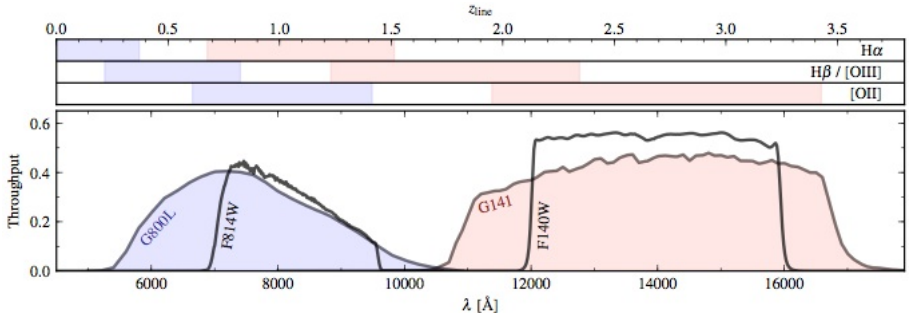

Figure 2.5: Throughput curve of WFC3-G141 (primary) e ACS/G800L (parallel) grism and imaging filters WFC3/F140W e ACS/F814W used to define the zero-point λ for each grism.
The upper stripes show the redshift intervals where spectral lines of $[OII]$, $H\beta$, $[OIII]$ e $H\alpha$ falls in the grisms' coverage (WFC3's in red and ACS's in blue).
From Brammer et al. (2012) [3]

The nominal G141 dispersion corresponds to $\leq$ 1000 km/s for Hα at $z > 1$ but one needs to take into account that the resolution of the slitless grism spectra is determined by the physical extent of a given object and by its orientation with respect to the dispersion direction.
The read noise of the WFC3/IR detector is $\sim 20\ e^-$, while the number of background electrons per pixel in a typical grism exposure is $1.4\ e^-$/s $\times$ 1300 s = $1820\ e^-$.
The effective continuum and emission line sensitivities of 3D-HST were evaluated by HST's team using a suite of simulations that is tied closely to the observed F140W direct and G141 grism exposures.
They generate a 2D model spectrum based on the spatial distribution of flux as determined in the F140W direct image, and an assumed input 1D spectrum, normalized to the F140W flux. They assume a simple continuum, flat in units of f_λ , combined with a single emission line at 1.3μm (i.e., Hα at z = 1). The emission line has a fixed equivalent width of (arbitrarily) 130 Å, observed-frame, and the overall normalization of the spectrum (and thus the integrated line flux) is set to the $FLUX_{AUTO}$ flux measured by SExtractor on the F140W image. They add realistic noise to the simulation considering for noise variations as a function of background level across all of the available pointings, and, most importantly, for the true distribution of source morphologies as a function of brightness within the 3D-HST survey. After computing the full grism image models, they extract individual spectra and the emission line strengths.

The uncertainties on the line fluxes are determined with a Markov Chain Monte Carlo ($MCMC$) fit of the line and a continuum template combination.
The average sensitivity of the survey was estimated to be $f_\lambda = 5.5 \times 10^{-17} erg/s/cm^2$. For the optimal case of point sources and the minimum background, the 5σ continuum and line limits are approximately 23.7 mag and $2.3 \times 10^{-17} erg/s/cm^2$.
Due to the low spectral resolution, Hα and $[NII]_{\lambda 6550+6584}$ are not resolved and the Hα line measurements represent the sum of these line species. The G141 spectral resolution tends to be just sufficient to produce an asymmetrical profile for the $[OIII]_{\lambda 4959+5007}$ doublet, which can help in differentiating it from Hα assuming that the profile of the line-emitting region is roughly symmetric.
The precision of the redshift measurements depends somewhat on the strength and availability of emission lines in the grism spectra.

The F140W filter

To establish the wavelength zero-point of the spectra, the observations with the HST grisms typically require an accompanying image. These so-called "direct" images for the G141 grism are obtained in the broad F140W filter that spans the gap between the standard J and H passbands and lies roughly in the center of the G141 sensitivity.
These direct images can also be useful for scientific analysis, as they reach depths competitive with even the deepest ground-based surveys (H $\leq$ 26.1, 5σ) with spatial resolution of $\leq 0.13''$ (Brammer et al. (2012) [3]).
The 5σ depth of the F140W detection images is H140 $\leq$ 26.1 for point sources within a $0.5''$ diameter aperture, varying by ± 0.3 mag due to the field-dependent background levels.

Chapter 3

Sample selection

In this chapter we describe the sample selection procedure that was realized matching an Herschel far-IR sample with the 3D-HST spectroscopic data-set.
We select our sample in the Great Observatories Origins Deep Survey South (*GOODS-S*) because in this field are available photometric observations in a broad range of wavelengths and this field has the deepest sampling with PACS-Herschel photometry at 70, 100 and 160 μm. We consider objects with a wide range of photometric data to address a detailed analysis about the Spectral Energy Distribution of each galaxy in the sample.
To connect HST detected sources with PACS objects, we take advantage of the GOODS-MUSIC catalog, an high quality multi-wavelength catalog that collects the available photometry for the objects detected in the GOODS-Southern field in a wide range of λ, from UV to IR. The use of this catalog is fundamental for the process of association since the Herschel's beam is not directly comparable to the high resolution imaging of HST. In particular, the inclusion of MIPS photometry at 24 μm is fundamental for our correlation due to the intermediate angular resolution of Spitzer with respect to Herschel and HST.
The MUSIC photometry was used also to build up our Spectral Energy Distribution, with the inclusion of the IRS data at 16 μm (Teplitz (2007) [46]). We refer to the 5^{th} chapter for the description of the SED fitting.

3.1 Multi-wavelength photometry: the GOODS-MUSIC catalog

The GOODS-MUltiwavelength Southern Infrared Catalog (*GOODS-MUSIC*) catalog (Grazian et al. (2006) [15]) contains magnitude data for the sources detected in the GOODS Southern area in z and Ks bands and it is entirely based on public data. Table 3.1 lists the filters used to acquire the photometric data.

FILTER	λ_c	$\Delta\lambda$	EXPTIME	*FWHM*[a]	PIXSCALE	ZP	AREA	MAGLIM[b]
	Å	Å	s	arcsec	arcsec/px	AB	arcmin^2	90%
U_{35}	3590	222	53 654	0.90	0.23	28.520	143.2	25.5
U_{38}	3680	170	75 100	1.10	0.23	28.755	143.2	24.5
U_{VIMOS}	3780	197	10 000	0.80	0.20	32.500	90.2	26.5
B ($F435W$)	4330	508	7200	0.12	0.03	25.65288	143.2	27.5
V ($F606W$)	5940	1168	6000	0.12	0.03	26.49341	143.2	27.5
i ($F775W$)	7710	710	6000	0.12	0.03	25.64053	143.2	26.5
z ($F850LP$)	8860	554	12 000	0.12	0.03	24.84315	143.2	26.0
$J_{\rm ISAAC}$	12 550	1499	12 600[c]	0.45[c]	0.15	26.000	143.2	24.5
$H_{\rm ISAAC}$	16 560	1479	18 000[c]	0.45[c]	0.15	26.000	78.0	24.3
$Ks_{\rm ISAAC}$	21 630	1383	23 400[c]	0.45[c]	0.15	26.000	143.2	23.8
$CH1_{\rm IRAC}$	35 620	3797	82 800	1.60	0.60	22.416	143.2	24.0
$CH2_{\rm IRAC}$	45 120	5043	82 800	1.70	0.60	22.195	143.2	23.4
$CH3_{\rm IRAC}$	56 860	6846	82 800	1.90	0.60	20.603	143.2	22.0
$CH4_{\rm IRAC}$	79 360	14 797	82 800	2.00	0.60	21.781	143.2	22.0

Figure 3.1: List of filters used to build up the photometric catalog. From Grazian et al. (2006) [15]

The catalog was produced with a specific software, built to perform an accurate PSF matching for space and ground-based images of different resolutions and depths. The catalog includes 14847 objects.
The photometric catalog was cross-correlated with a master catalog[1] released by the ESO-GOODS's team, that summarizes all the informations about spectroscopic redshifts in the GOODS area collected from several surveys. For the sources lacking a spectroscopic measurement, a photometric redshift was computed using a code that is based on a standard χ^2 technique on a set of synthetic templates.
The MUSIC catalog was extended (Santini et al. (2009) [42]) with the inclusion of the mid-infrared fluxes, obtained from MIPS observations at 24 μm. This inclusion was very useful for the association with the Herschel's data, due to the fact that Spitzer has an intermediate resolution between optical instruments and the Herschel Space Telescope. In particular, the PACS catalogs selected with priors at 24 μm (for more

[1] www.eso.org/science/goods/spectroscopy/CDFS_Mastercat/

details about the catalog we remind at section 2.2) were associated with the ancillary photometric informations with a maximum likelihood procedure, starting from 160 μm and progressively cross correlating with observations at 100 μm, 70 μm and 24 μm.
Therefore we have a catalog of PACS-MUSIC sources, selected at 100 and/or 160 μm and composed by 631 objects with fluxes higher than 192.5 mJy at 100μm and higher than 233.6 mJy at 160 μm.

3.2 Cross correlating the Herschel and HST samples

Starting from the PACS catalog, we perform the cross correlation procedure with the 3D-HST observations, using the IRAC coordinates of the PACS sample.
We performed a cross-correlation in RA and Dec using the matching algorithm "Sky" in TopCat with a matching radius of $2\,arcsec$. The cross-correlation procedure leads to 378 PACS objects with a counterpart in the 3D-HST observations.

3.2.1 Cleaning of the sample

In order to consider only objects with strong Hα emission we perform a visual check of each spectrum to discard objects without any emission line features or to exclude faint or saturated sources. To identify only an Hα emission line we used as an estimate of redshift the information contained in the MUSIC catalog and so we excluded from our sample sources that show other emission line features as [OIII] emission line.
The reason to select only the Hα line is that this well calibrated estimator of SFR traces the youngest episodes of stellar formation activity and it is metallicity independent and less affected by extinction than other emission lines associated to heavier elements.
To perform this visual check on the spectrum we used the IDL routine ***extract_grism_spec.pro***, written by Kevin Shawinsky. For more details about the routine see the next chapter.

One of the problems connected to slitless spectra is the correct association between the object's position and its spectrum, due to the high contamination in the field that often produces an overlap with different order of spectra from other sources.

In order to verify the right connection between each source and its spectrum, we did a visual check with the interactive image display tool Graphical Astronomy and Image Analysis Tool (*GAIA*) on the pointing images.
We have firstly cross-correlated objects positions with the direct imaging so we identified the location of our galaxies on the pointings. Later, the image of the pointing with a flag for each detected objects was superimposed on the grism exposure for each pointing through a contour plot, as shown in figure3.2.1 which contains an example for the pointing 7. The contour plot was compared with the imaging of each source in the H-F125W HST broad band and the associated frame with the 2D spectrum. We see in the figure 3.3 the 3D-HST spectrum for the source 9452, while figure 3.4 shows the H-band image for the same object.

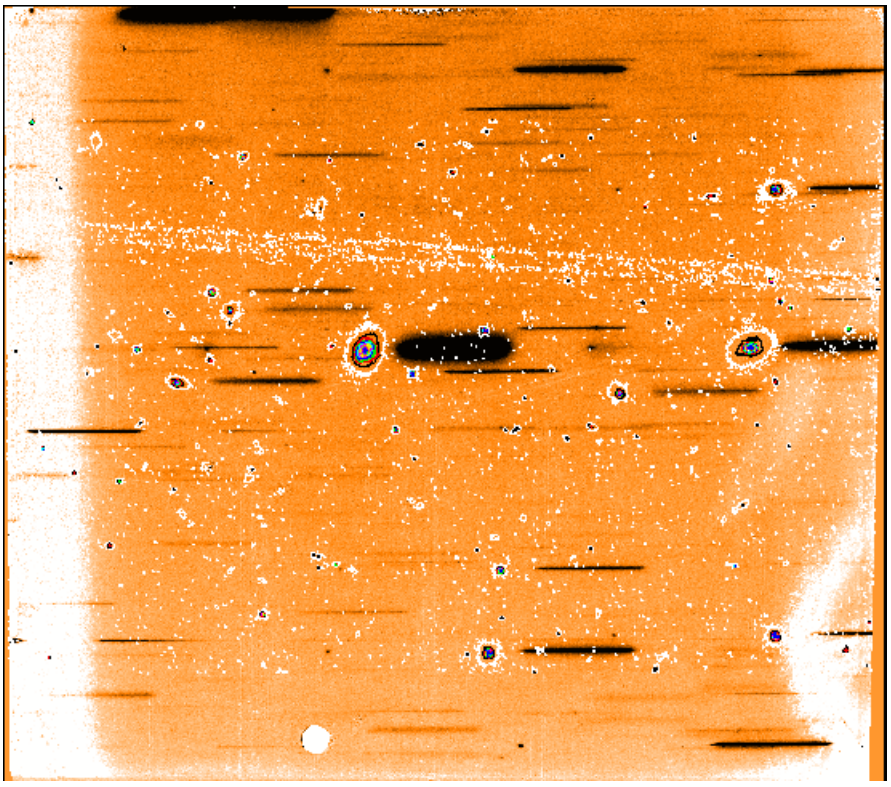

Figure 3.2: Pointing 7 of the G141 grism image. The direct F140W image is superimposed on the grism image through a contour plot to identify the sources in the sample and check the association between each galaxy and its spectrum.
The image has a scale of $0.13 arcsec/pixel$. North is down and East is right.

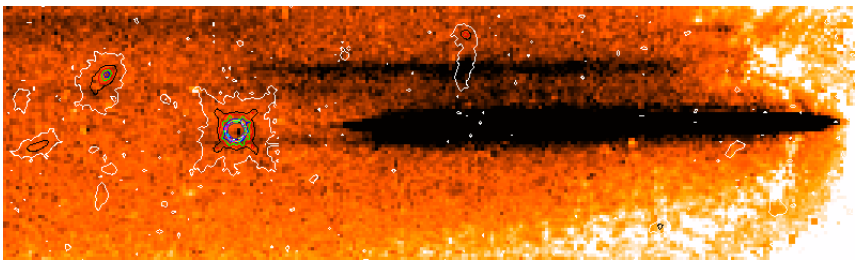

Figure 3.3: Zoom of the pointing 7 (Figure 3.2.1) of the G141 grism spectra which contains the 2D spectrum of the source 9452.

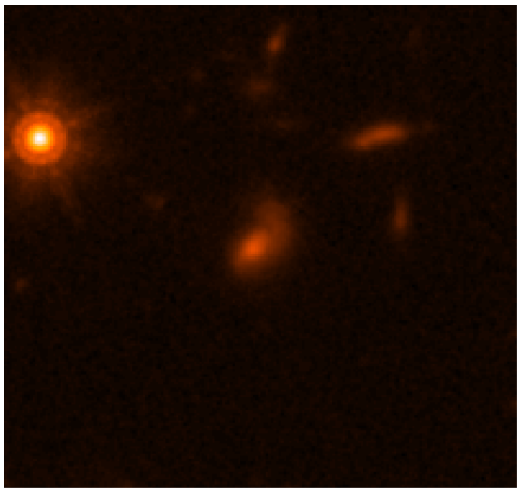

Figure 3.4: WFC3/combined image for source 9452 in the F125W filter (HST-H broad band). The cutout was acquired from the Hubble Legacy Archive.
The frame has a scale of $0.06 arcsec/pixel$. North is up, East is left.

The catalog consists of 98 objects with a wide range of photometric data. About 40% of these objects have ground-based spectroscopic redshift in the MUSIC catalog. We refer to the next chapter for the estimate of the redshifts from the 1D spectra.
Figure 3.5 shows the evolution of the total infrared luminosity L_{IR} as a function of redshift. The infrared luminosity L_{IR} is derived from the SED fitting (see the 5^{th} chapter for more details about the procedure) while the redshifts are derived from the 3D-HST spectra (see the following chapter for details about the computation). We can observe that the selected sources show quite high values of L_{IR} ($\Delta L_{IR} \sim [4.9\times10^{10} - 2.5\times10^{12}] L_{\odot}$, median $L_{IR} \sim 2.7\times10^{11} L_{\odot}$), as expected for an Herschel far-IR selected sample.

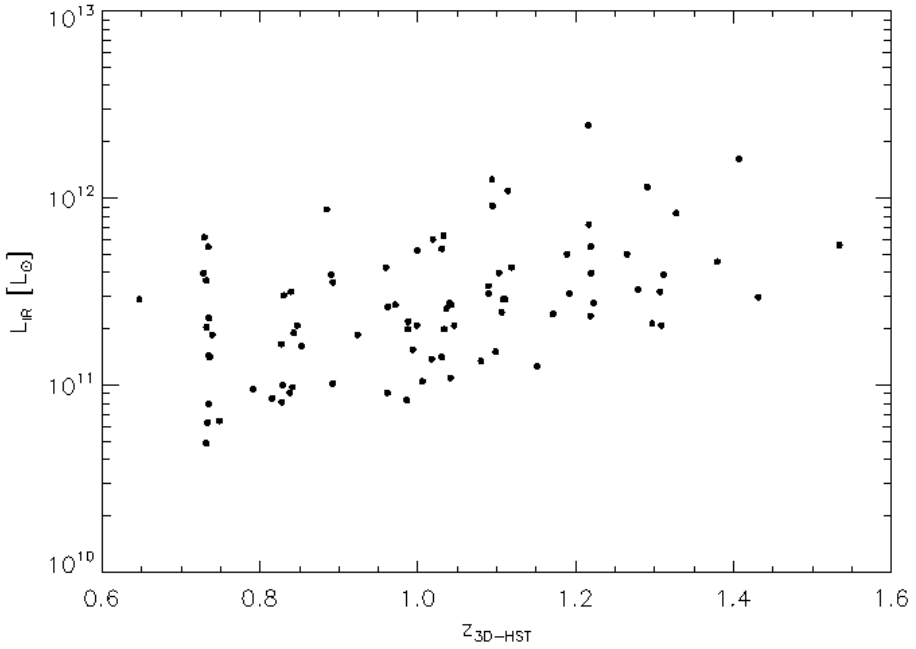

Figure 3.5: Total infrared luminosity L_{IR} ($\lambda \in [8-1000]\mu$m) as a function of redshift for the 3D-HST sources.
L_{IR} is derived from the SED fitting while the redshift measurements here considered are computed from the 3D-HST near infrared spectra.

Chapter 4

Analysis of the 1D HST slitless spectra

In order to compute measurements of Hα fluxes, we extract the mono-dimensional spectrum from the 2D grism spectrum collapsing it inside a specific aperture.
We used for the extraction the IDL routine ***extract_grism_spec.pro*** written by Kevin Schawinsky. This tool reads the frame with the image of the 2D spectrum, applies the wavelength and flux calibrations and extract a mono-dimensional spectrum. The extraction is performed inside a "virtual slit" that is defined by the two pixel's rows set up in input. The width and the position of the virtual slit are adjusted on each object in order to magnify the S/N ratio to clearly see the Hα emission against the continuum. An example of the plot generated by the routine is shown in figure 4.1.

In the first section of this chapter we summarize the calibration done by the 3D-HST team (for a detailed description of the procedure see Brammer et al. 2012 [3]). The other sections contain the description of our spectral analysis. We describe the extraction of the 1D spectra, the measurements of the Hα fluxes, the computation of spectroscopic redshifts and the estimate of the aperture corrections for the Hα fluxes.

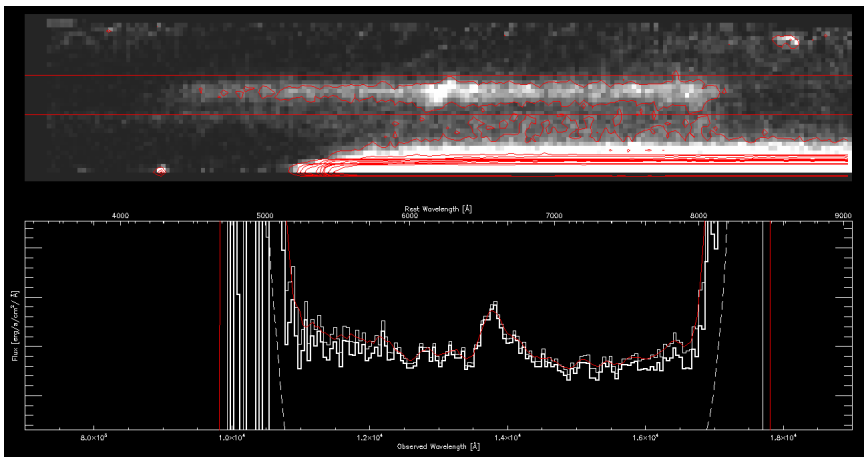

Figure 4.1: *Upper panel:* image of the 3D-HST bi-dimensional spectrum for source 9452, as displayed by the IDL routine ***extract_grism_spec.pro***. The red horizontal lines define the "virtual slit". The second bright spectrum down on the right is associated with another source.
*Lower panel:*1D spectrum of source 9452, obtained collapsing the 2D spectrum along the columns inside the virtual slit. The flux is in $erg/sec/cm^2/$Å, the wavelength in Å. The red solid line is the scientific spectrum, while the white dashed line is the contamination from nearby sources. We see in the central part of the spectrum the Hα emission.

4.1 HST calibration

The IDL routine reads and applies the calibration files prepared during the reduction processes by the 3D-HST's team.

The 248 3D-HST orbits are divided among 124 individual visits of two orbits each. Each of the 3D-HST two-orbit visits with WFC3 is structured in an identical fashion: four pairs of a short F140W direct image (we remind that a direct image is an image required to establish the wavelength zero-point of the grism spectrum, as already explained in section 2.2.1.1 of the previous chapter) followed by a longer G141 grism exposure. The four pairs of direct+grism exposures are separated by small telescope offsets to enable the rejection of hot pixels and pixels affected by cosmic-rays, as well as dithering over some WFC3 cosmetic defects such as the "IR-blobs".
The 3D-HST team uses as a starting point the standard calibrated data products provided by the HST archive that have been processed by the *calwf3* reduction pipeline for the WFC3. The calibrated WFC3/IR images have 1014×1014 pixels, with roughly 0.128 $arcsec/pixel$.
Briefly, the calibration pipeline flags known bad pixels in the data quality image extensions, subtracts the bias structure, the overscan regions,

dark current, and applies multiplicative corrections for the detector gain. A more comprehensive description of the WFC3 reduction pipelines is given by Koekemoer et al. (2011) [24].
To identify any hot pixels or cosmic rays not flagged by the instrument calibration pipeline, it was used the *MultiDrizzle* software.
Small adjustments to the commanded telescope dither offsets are determined using the PyRAF routine, *tweakshifts*. These shifts are at most 0.1 pixels.
The WCS coordinates of the mosaic image with respect to a WCS reference image were refined by matching object catalogs extracted from each image and fitting for shifts and rotations using the IRAF task, *geomap*. The derived image rotations are typically less than 0.1 *deg* and the *rms* of the shifts matched between the catalogs is generally $\sim$0.1 pixel (0.006").
Once the relative and offset shifts are determined for the direct images, the grism exposures are assigned the same shift as their preceding direct image, assuming that there was no shift between the two exposures.
The near-IR background flux is a significant component also in low-Earth orbit and must be subtracted from both the direct and grism exposures. For the direct images the background is subtracted with a second-order polynomial fit to each exposure. To correct the grism exposures for the background it was created a "master grism" background image, starting from the (masked) average of many grism exposures, that then is scaled to and subtracted from each grism exposure. This is the approach followed by the aXe software package (Kummel et al. (2009) [26]).
The aXe package was also used to extract the grism spectra with two inputs: a detection image mosaic and the individual background-subtracted grism exposures generated. An object catalog is generated from the detection image with the SExtractor software (Bertin & Arnouts (1996) [2]), which also produces a segmentation map that indicates which pixels in the direct image are assigned to each object. For a given pixel within a particular object's segmentation map, the calibration of the HST grisms determines where the dispersed light from that pixel will fall on the grism exposures, with the pixel in the direct image defining the wavelength zero-point for the spectrum. Thus, the grism spectrum of an object is the sum of all of the dispersed pixels within that object's segmentation image, or rather, the spectrum is a superposition of the object profile at different wavelengths offset by the grism dispersion. The effective spectral resolution is therefore a combination of the grism dispersion and the object profile in the sense that the effective resolution decreases with increasing object size in the dispersion direction.
As there is no slit defining a spatial axis, an "effective slit" running roughly parallel to the major axis of each object is not generally par-

allel to the y pixel direction in the undistorted frame. To optimize the wavelength resolution of the extracted spectra one need to consider the orientation of the major axis of each object against the dispersion direction and the shape of the sources. We ignore these effect for simplicity and we consider as dispersion solution its mean value.
Because no slit mask is used and the length of the dispersed spectra is larger than the average separation of galaxies down to the detection limit of the 3D-HST survey, the spectra of nearby objects can overlap. This "contamination" of an object's spectrum by flux from its neighbors must be carefully accounted for in the analysis of the grism spectra. With the aXe software it was produced a full quantitative model of the grism exposure, starting from the information in the direct image. This is the aXe "fluxcube" contamination model, which makes use of the spatial information contained in the high-resolution HST images to model the two-dimensional grism spectrum.

4.2 Hα fluxes and redshift measurements

The routine requires in input two pixel rows which define a "virtual slit" that is the frame region where the 1d spectrum is extracted. The size of the virtual slit was defined on each source's spectrum to magnify the S/N.
The mono-dimensional spectrum is determined by adding the flux of the source for each pixel along columns between the two bounds of the virtual slit from the bi-dimensional spectrum in input. The routine plots and subtracts from the scientific spectrum also the contamination spectrum and the background as estimated by aXe.
The 1d spectrum shows border effects, the so-called "ears" that are not a real component of the spectrum itself: these arise from the fact that the sensitivity for extended sources is not constant along the Field of View and the mean sensitivity function here applied is calculated on point sources. During the subsequent analysis we simply cut this part of the spectrum.

For each object in our sample we will provide a redshift measurement and an integrated flux estimate from the analysis of the Hα emission in the 1d spectrum.
Each of the 1d spectra extracted from the bi-dimensional spectrum was analyzed with the IRAF's task ***splot*** to obtain Hα fluxes fitting the emission line with a Gaussian function. ***Splot*** is an interactive facility to display and analyze spectra. It allows to interactively mark two con-

tinuum points around the line and fit this line with a Gaussian profile assuming the underlying continuum to be constant. The fitting uses an iterative algorithm based on the Levenberg-Marquardt method.
In a slitless spectrum the grism produces an emission line image that is superimposed onto a sequence of disperse monochromatic images of continuum. The width of lines is not only caused by velocity broadening (negligible at low resolution, as 3D-HST spectra are) and by the intrinsic broadening of the λ dispersion: as slitless spectroscopy produces shifted monochromatic images, the spatial extent of the dispersed emission line image reflects the spatial distribution of the line emission both along and perpendicular to the dispersion direction ("morphology" broadening, Schmidt et al. (2013) [43]). Because the spatial resolution of the WFC3 detector is greater than the spectral resolution, the spectral line profiles are so dominated by the object shapes and the grism line shapes are not well described by Gaussian profiles but we use this kind of fitting for convenience.
Splot computes some parameters for each line: the center position, the continuum at the center, the core intensity, the integrated flux, the equivalent width, the σ of the Gaussian profile and the full width at half maximum. Each parameter, except the continuum, are based on the analytic Gaussian profile. ***Splot*** provide also an error estimate for the measured parameters. This requires a model for the pixel σ: currently this is based on a Poisson statistics model of the data. The model parameters are a constant Gaussian σ and an inverse gain: these parameters are used to compute the pixel value σ.

$$\sigma^2 = \sigma_0^2 + invgain * I \tag{4.1}$$

where I is the pixel value. Here we use a constant noise, setting $invgain$ to zero and determining σ_0 for each object from the continuum near the emission line.
Gaussian fit error estimates are computed by MonteCarlo (MC) simulation. The model is fitted to the data and this model is used to describe the noise-free spectrum. The number of simulation with random Gaussian noise can be set in input. We compute the errors with 50 iterations of the MC simulation. The model fitting is done for each simulation and the absolute deviation of each fitted parameter to model parameter is recorded. The error estimate for each parameter is then the absolute deviation containing 68.3% of the parameter estimates (1σ if the distribution of parameter estimates is Gaussian).
From the value of the center of the lines in output we compute the measurements of redshifts. In order to confirm the precision of our estimates

we compare the 3D-HST's redshifts with the MUSIC values. We found that the measurements are in good agreement with the pre-existing redshift values.

For 11 objects in our sample with spectroscopic MUSIC redshift the measurements are in disagreement: we classify these objects as peculiar and we excluded them from the subsequent analysis so the final sample consists in 87 galaxies with strong $H\alpha$ emission. The causes of these outliers include misidentification of single emission lines, poor background and/or contamination subtraction of the G141 spectra and apparent errors of the spectroscopic redshifts themselves.

We compute the redshift distribution for our sample and the correlation with z_{MUSIC} values. The redshifts are distributed between 0.7 and 1.5, according to the grism+filter transmission that can detect an $H\alpha$ emission in this redshift interval. The z-distribution is reported in figure 4.2.

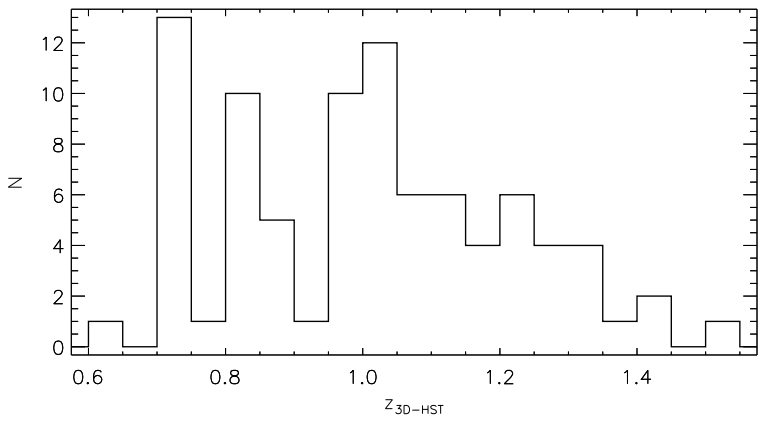

Figure 4.2: The redshift distribution for the 3D-HST sources in the GOODS Southern field. It shows two peaks, at z∼0.7 and z∼1. The sources are distributed in a redshift interval $z \in [0.6 - 1.5]$, according to the features of the WFC3/G141 grism.

The correlation between the redshift measurements is shown in fig 4.3. The correlation works pretty well also for the photometric estimates of redshift (red dots): this behavior stresses the validity of the method of photometric redshifts.
We consider the z_{3D-HST} as the best estimate of redshift for our sources and we will use these measurements for the subsequent work.

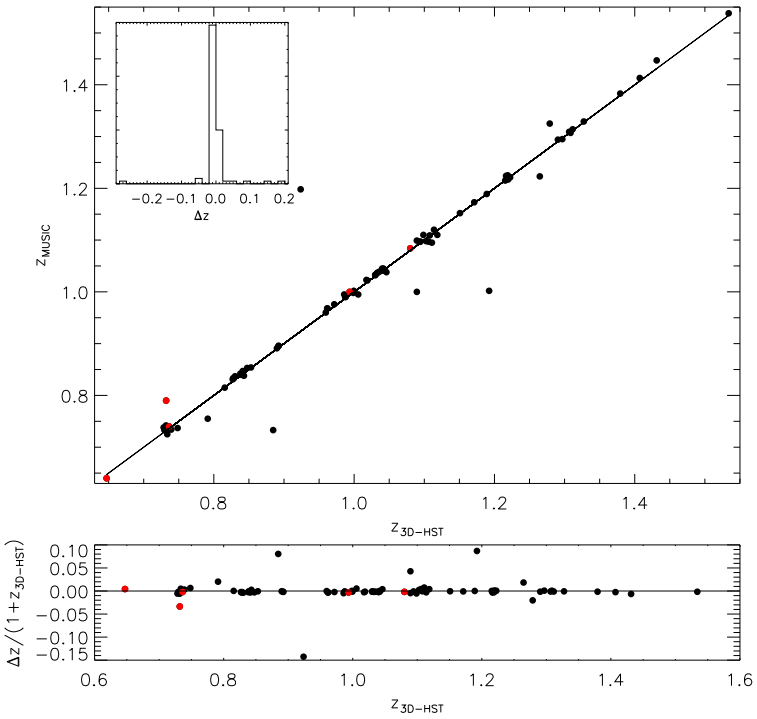

Figure 4.3: *Upper panel:* the relation between 3D-HST spectroscopic redshifts (x-axis) and MUSIC redshifts for the objects in the sample. In the inset, the distribution of the absolute scatter $\Delta z=(z_{3D-HST}\text{-}z_{MUSIC})$ is shown. The standard deviation for this distribution is σ=0.042. *Lower panel:* relative scatter $(z_{3D-HST}\text{-}z_{MUSIC})/(1+z_{3D-HST})$.
The data points in red are the photometric measurements in the MUSIC catalog, the black dots are the sources with spectroscopic redshift also in the MUSIC catalog from ground based measurements.

4.3 Aperture corrections

The position and the width of the virtual slit used to extract the 1d spectrum from the bi-dimensional image are adjusted on each object in order to magnify the S/N ratio. We need to compute aperture correction to account for flux losses outside the slit. We applied two different methods. We compute the aperture corrections from the curve of growth, building this one from HST imaging in H band. We also calculate a scaling factor for each object from its SED, computing a mean flux from the 1d spectrum continuum and a mean flux from the SED in the same range of wavelength.

4.3.1 The curve of growth

The first of the two methods used to derive the aperture corrections is based on the computation of the curve of growth. We calculate for each object in the sample the photometry inside circular apertures centered on the object, in order to estimate the trend of the source's flux versus its radius.
We acquire the cutout images for each galaxy from the Hubble Legacy Archive[1]. A cutout is a view of a small portion of an image, centered at the RA/Dec position specified in the search. The size of each downloaded cutout is 10 *arcsec* and it is centered around the MUSIC coordinates of each galaxy. We used combined images from WFC3-F125W observations so these images are in the HST broad H-band (the nearest to the rest frame Hα emission) and have a pixel scale that can change from 0.09 *arcsec* to 0.06 *arcsec* depending on the reduction procedure.
To perform the aperture photometry we use SExtractor in "circular apertures" mode. This procedure allows us to compute photometry inside circular apertures with increasing diameters, specified by the user. To compute the extraction, we adopted the parameters listed in table 4.1. The parameters related to the background were set on the entire field because the cutout's size is too small and the estimate of these quantities on the frame is not representative of the real background. For each source we measure the flux inside 25 circular apertures. We show an example in figure 4.4: the left part of the image is the check image in output from SExtractor, with the circular apertures superimposed on the source; the right part of the image is the image in the F125W band.

[1] `http://hla.stsci.edu/`

PARAMETER	VALUE
DETECT_MINAREA	5
DETECT_THRESH	3σ
DEBLEND_NTHRESH	32
DEBLEND_MINCONT	0.005
CLEAN_PARAM	1.0
BACK_SIZE	64
BACK_FILTERSIZE	2
BACKPHOTO_THICK	25

Table 4.1: SExtractor parameters used to compute the aperture photometry.

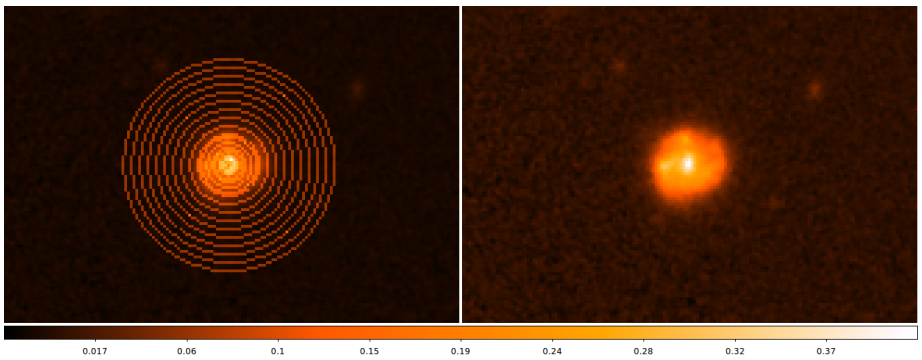

Figure 4.4: *Left:* The check image produced by SExtractor which shows the circular apertures used to perform the photometry. *Right:* Image of the source 3636 in the F125W band.
The scale of the image is $0.06 arcsec/pixel$. North is up, East is left.

From the SExtractor aperture photometry we compute for each object in our sample the curve of growth, interpolating the data-points with a spline function. Starting from this curve we evaluate the total flux associated to the object F_{tot} where the curve starts to flatten. We calculate also the flux inside the virtual slit F_{slit} as the flux inside an aperture which corresponds to the aperture in pixel used for the extraction of the 1D spectrum. In figure 4.5 we illustrate as an example the curve of growth for the source 3636 (figure 4.4).

The ratio F_{slit}/F_{tot} is the correction factor that will be multiplied to the spectrum to account for the source's flux that falls outside the aperture. This kind of method leads to several problem. At first, from SExtractor we computed fluxes inside circular apertures but the flux associated to the spectrum is calculated inside a rectangular aperture. We have also to point out that in some cases the slit is off center but the SExtractor apertures are always centered on the galaxy luminosity barycenter.
At least we must consider that the Hα luminosity may not trace the

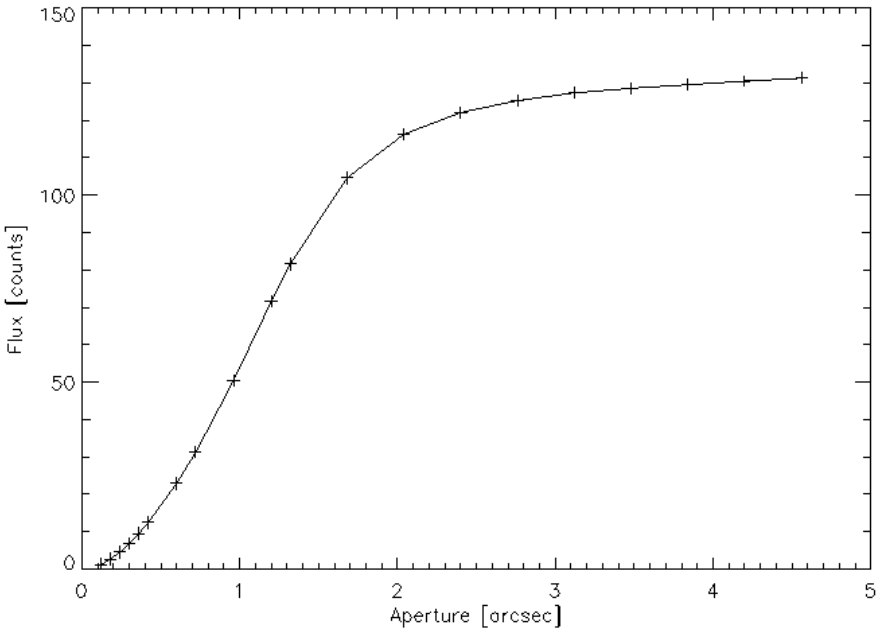

Figure 4.5: Curve of growth computed for the source 3636. In abscissa we report the radius in *arcsec* from the centroid of the object, in ordinate we report the flux inside each circular aperture in counts. The data points are fitted with a spline function.

continuum of the source. For this point, we have also to say that here we choose the H-band imaging to evaluate the photometry because this is the nearest band to the Hα rest-frame range for which we have reduced frames but, as observed by Wuyts et al [48], the Hα emission correlate with I-band more than the H-band.

4.3.2 SED scaling

The alternative method used to derive a correction factor for 1D spectra is based on the comparison between two continuum flux values, one estimated on the spectrum and the other evaluated on the best-fit model SED in the same wavelength range. For details about the SED fitting we refer to the next chapter.
For each object we estimate from a visual inspection on the 1D spectrum a wavelength range associated with the continuum emission, and here we calculate the mean continuum flux associated to the 1D spectrum, F_{spec}. In the same wavelength range where we compute the measure of F_{spec}, we evaluate the mean continuum flux on the spectral energy distribution F_{SED}. The ratio F_{spec}/F_{SED} gives the correction factor for the 1D spectrum and the Hα flux.

To test the validity of the methods used to compute the aperture corrections, we plot on the sources SEDs the near-infrared spectra multiplied for the aperture correction factors. We show two examples of the plots in figure 4.6.
For the correction factors derived from the aperture photometry we do not see any overlap between SED and spectrum, with an exception of a couple of objects. In general we see an overestimate of the total flux for the correction derived from the curve of growth. This behavior seems not to be related to the slit position on the 2D spectrum, neither to the strength and the extent of the Hα emission and stresses the intrinsic problem of this approach, as discussed above.
Applying the aperture correction factors derived from SED to the spectra we obtain a very good overlap between the near-IR spectrum and the SED for all the objects in the sample. We have to consider that for some sources some regions of the spectrum are not superimposed on the SED. This trend is due to the presence of other spectra near the selected sources that can cause high level of contamination. The contamination however does not involve errors in the estimate of the aperture correction factors: in this cases the mean flux associated to the spectrum is evaluated in a wavelength range linked to the selected source (this is the reason to use an adjusted $\Delta\lambda$ for each galaxy against a fixed range).

In table 4.2 we report the redshift, the size of the virtual slit and the aperture corrections for part of the sample. Table 4.3 contains the mean values of the size of the virtual slit and of the aperture corrections.

ID MUSIC	**Redshift**	**Slit [px]**	F_{slit}/F_{Tot}	F_{spec}/F_{SED}
10015	0.99	5	0.138	0.945
10263	1.32	4	0.077	0.601
10295	1.05	7	0.196	0.757
10617	1.44	4	0.265	0.900
10669	0.97	6	0.211	0.755
10681	1.18	5	0.161	0.604
10859	1.09	5	0.187	0.660
10972	0.84	4	0.080	0.477

Table 4.2: Aperture corrections for the first ten sources of our sample.

Mean Slit [px]	**Mean** F_{slit}/F_{Tot}	**Mean** F_{spec}/F_{SED}
7.24	0.26	0.81

Table 4.3: Mean values for the virtual slit and the aperture corrections.

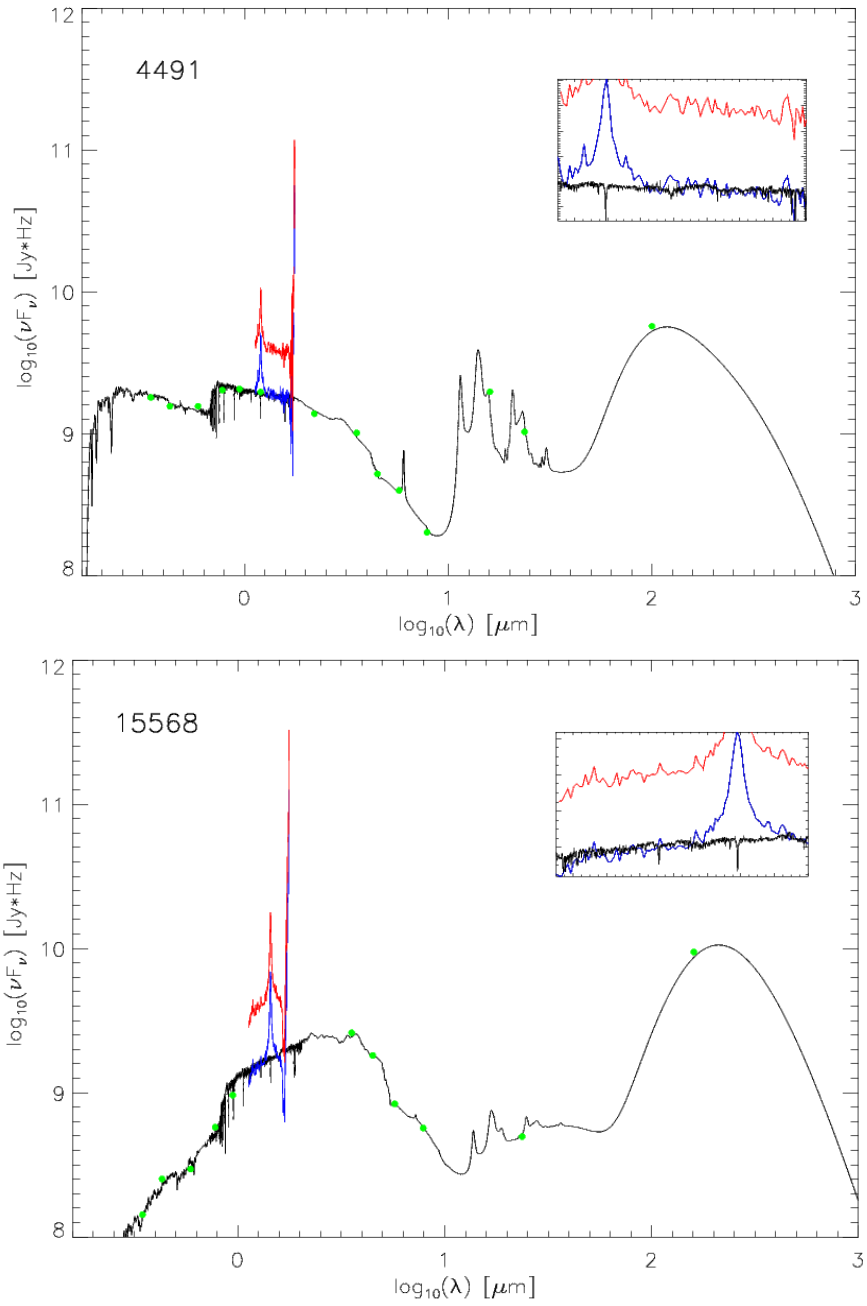

Figure 4.6: Theoretical spectral energy distribution of the sources 4491 and 15568, computed from MAGPHYS. The blue solid line is the 3D-HST near infrared spectrum scaled on the SED. The red solid line is the same spectrum multiplied with the factor derived from the curve of growth. The green dots are the observed photometric points. All the spectra are plotted in the observed-frame. The inset contains the zoom on the Hα emission line.

Chapter 5

The Spectral Energy Distributions

The Spectral Energy Distribution (*SED*) of a galaxy contains valuable information about its physical properties, including the stellar, gas and dust content, the age and abundance distribution of the stellar populations resulting from the Star Formation History (*SFH*), and their interactions with the interstellar medium (*ISM*). The study of the SED therefore offers the most direct way to investigate galaxy formation and evolution, both through direct observations and corresponding theoretical modeling. The different physical processes occurring in galaxies all leave their imprint on the global and detailed shape of the spectrum, each dominating at different wavelengths. Therefore, by analyzing and predicting the whole spectral range, one can hope to deconvolve and interpret all the information contained in the SED, in terms of the SFH and galaxy evolution in general (Lo Faro et al. (2013) [28]).
In order to analyze the physical properties of the galaxies in our sample, in particular the features of dust and its impact on each galaxy spectrum and on the SFR estimate, we compute the Spectral Energy distribution for each selected object. The SEDs allow us also to derive the corrections factor for the 1D-HST spectra and to test the validity of the two methods applied, as already discussed in section 4.3.
In this work we compute the theoretical SEDs with the model package Multi-wavelength Analysis of Galaxy Physical Properties (*MAGPHYS*, da Cunha , Charlot & Elbaz (2008) [8]) that is optimized to derive statistical constraints of fundamental parameters related to star formation activity and dust content (e.g. star formation rate, stellar mass, dust attenuation, dust temperatures) of large samples of galaxies.

MAGPHYS is build up to interpret multi-λ observations of galaxies in terms of the physical parameters pertaining to the stars and the interstellar medium. MAGPHYS compares the observed fluxes for each galaxy in the sample with a large library of reference galaxy spectra, sampling wide ranges of star formation histories, metallicities and dust contents to build up the marginalized likelihood distribution of each physical parameter of the observed galaxy.
To assess the emission from stellar population in galaxies, MAGPHYS uses the Bruzual & Charlot (2003) [4] stellar population synthesis code, adopting a Galactic disc IMF of Chabrier (2003) [6]. The model of Bruzual & Charlot is based on the property that stellar populations with any star formation history can be expanded in a series of instantaneous burst, "simple stellar populations" (*SSPs*). The spectral energy distribution of a galaxy is then computed by adding the individual spectra of all *SSPs* weighted by the star formation rate over time since the galaxy was formed.
The infrared emission from galaxies is generally related to three main constituents of interstellar dust:

- *PAHs*, which produce strong emission features at near-infrared wavelengths.
- grains with sizes typically less than 0.01 μm, which are stochastically heated to high temperatures by the absorption of single UV photons and emit at mid-infrared wavelengths (*hot dust*).
- big grains with sizes typically between 0.01 and 0.25 μm which are in thermal equilibrium with the radiation field and dominate the galaxy emission at far infrared wavelengths (*warm* and *cold grains*).

MAGPHYS models the infrared SED of a galaxy using two main components: the *ambient (diffuse) interstellar medium* with emission coming from PAHs, hot dust, warm and cold grains and the star-forming regions *birth clouds*, with emission coming from PAHs, hot dust and warm grains. The infrared emission is based on the angle-averaged model of Charlot & Fall (2000) [7] that accounts for the dissipation of molecular clouds on a time-scale of $t_0 \sim 10^7\ yr$. The result of this dissipation is that the non-ionizing continuum emission from young OB stars and line emission coming from their surrounding HII regions may be absorbed by dust in these birth clouds and then in the ambient ISM, while the light emitted by stars older than $10^7 yr$ propagates only through the diffuse ISM. The model so accounts in this way for the different attenuation of line and continuum emission in star-forming galaxies. The figure 5.1 shows a model infrared SED from MAGPHYS.

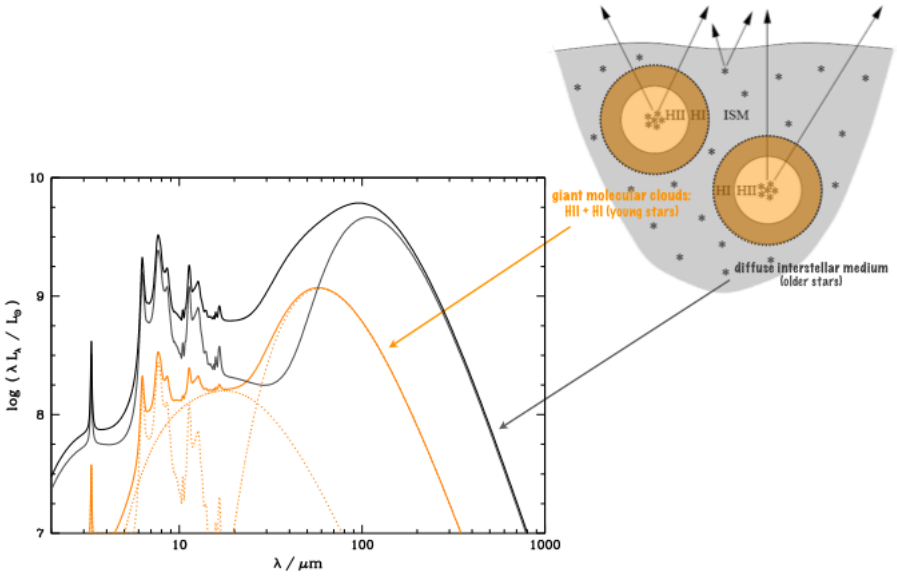

Figure 5.1: Example of model infrared SED showing the emission by the birth cloud (orange) and the diffuse ISM (grey) component. From `http://www.iap.fr/magphys/magphys/MAGPHYS.html`

The main feature of MAGPHYS is the consistent interpretation of UV, optical and IR SED of galaxies, linking the optical and IR libraries in a physically consistent way.
This is achieved by first computing the total energy absorbed by dust in stellar birth clouds and in the ambient ISM and then redistributing it at infrared wavelengths. The main assumptions are the conservation of the energy absorbed and re-radiated by dust and that the dust in the ISM of galaxies is heated only by starlight. The main underlying assumptions are that the energy re-radiated by dust is equal to that absorbed (energy conservation) and that starlight is the only significant source of dust heating (e.g. any AGN's contribution is ignored).
The absorbed energies can be distributed in wavelength using different combinations of dust parameters in the stellar birth clouds and the ambient ISM. To derive statistical constraints on the various parameters, MAGPHYS considers a wide library of models encompassing all plausible parameter combinations. For each observed galaxy it is build the likelihood distribution of any physical parameter by evaluating how well each model in the library can account for the observed properties of the galaxy.

The physical parameters in output are:

- f_μ the total infrared luminosity contributed by dust in the ambient ISM
- τ_V the total effective V-band absorption optical depth of dust
- μ fraction of the total V-band absorption optical depth of the dust contributed by the ambient ISM
- $\mu\tau_V$ effective V-band absorption optical depth of the dust in the ambient ISM
- ψ_s the specific star formation rate
- M_* the stellar mass
- M_{dust} the dust mass
- L_d^{tot} the total infrared luminosity of the dust in the wavelength range between 8-1000 μm
- ξ_{PAH}^{tot} the global contributions (i.e. including stellar birth clouds and the ambient ISM) by PAHs to the total infrared luminosity
- ξ_{MIR}^{tot} the global contributions (i.e. including stellar birth clouds and the ambient ISM) by the hot mid-infrared continuum to the total infrared luminosity
- ξ_W^{tot} the global contributions (i.e. including stellar birth clouds and the ambient ISM) by the warm dust in thermal equilibrium to the total infrared luminosity
- T_W^{BC} the equilibrium temperature of warm dust in stellar birth clouds
- ξ_C^{tot} the contributions by cold dust in thermal equilibrium to the total infrared luminosity
- T_C^{ISM} the equilibrium temperature of cold dust in the ambient ISM

The main parameters of interest for the present work are the Star Formation Rate, the total infrared luminosity L_d^{tot}, the stellar masses M_* and the dust masses M_{dust}.

To compute the SED fitting for our sample we use photometric data in 16 bands from the U band to the far Infrared wavelengths. Table 5.1 lists the filters used for the SED fitting. We compute the SEDs using our spectroscopic estimate of the redshift, derived from the 3D-HST near-infrared spectra.

Filter	λ_{eff} [μm]
U	0.346
ACSF435W	0.4297
ACSF606W	0.5907
ACSF775W	0.7774
ACSF850LP	0.9445
ISAACJ	1.2
ISAACH	1.6
ISAACK	2.2
IRAC1	3.55
IRAC2	4.493
IRAC3	5.731
IRAC4	7.872
IRS16	16
MIPS24	23.68
PACS100	100.
PACS160	160.

Table 5.1: List of the 16 filters used to perform the SED fitting and respective effective wavelengths λ_{eff}.

The lack of data in the mid-IR leads to difficulties in measuring the temperatures of the diffuse ISM T_C^{ISM} and the temperature of the birth cloud T_W^{BC} as shown in figure 5.2: the likehood distribution for both parameters is in fact nearly flat. The inclusion of the photometric data at 16μm is not sufficient to constrain these values.

The χ^2 values for the SED fitting are in general lower than 1 so on average the fitting for the sample is good. However there are 10 sources for which the fit is bad. In five cases the problem seems related to an outlier photometric data point and the quality of the fit is improved excluding this value. For the other five sources there is a luminosity excess in the near-IR and mid-IR part of the rest-frame spectrum: this can be due to the possible presence of an AGN. An example of this kind of SED is shown in figure 5.3 for source 12354. We report also the H-band image (Figure 5.4) and the 3D-HST spectrum (Figure 5.5) of the object 12354. The imaging shows a very strong point source and the spectrum has a strong and broad Hα emission.

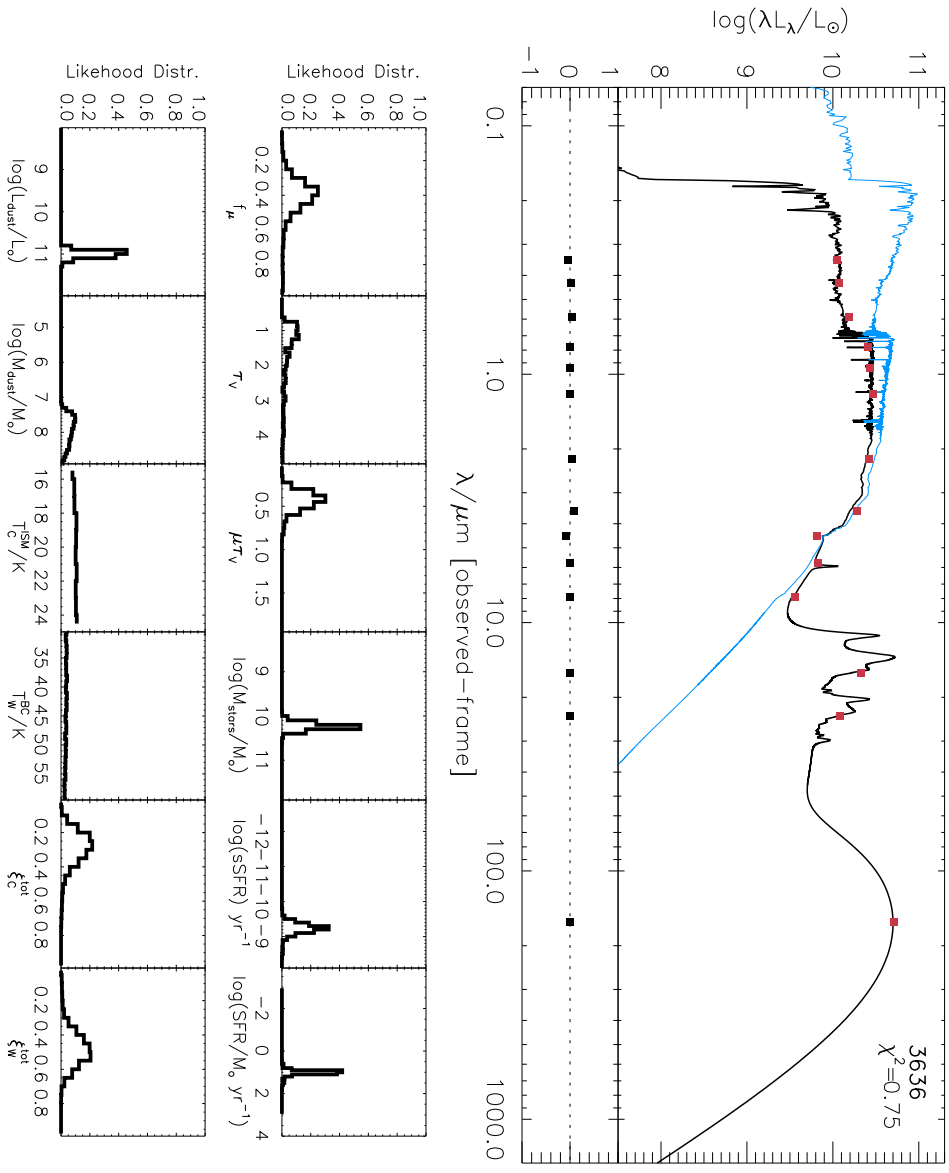

Figure 5.2: Example of a Spectral Energy Distribution in output from MAGPHYS. The black solid line is the best-fit model to the observed SED (data-points in red). The blue solid line shows the unattenuated stellar population spectrum. For each observational point, the vertical error bar indicates the measurement error, while the horizontal error bar shows the effective width of the corresponding photometric bands. The bottom panel shows the residuals $(L_\lambda^{obs}$-$L_\lambda^{mod})/L_\lambda^{obs}$. The histograms below show the likelihood distribution of the physical quantities derived from the fit to the observed SED.

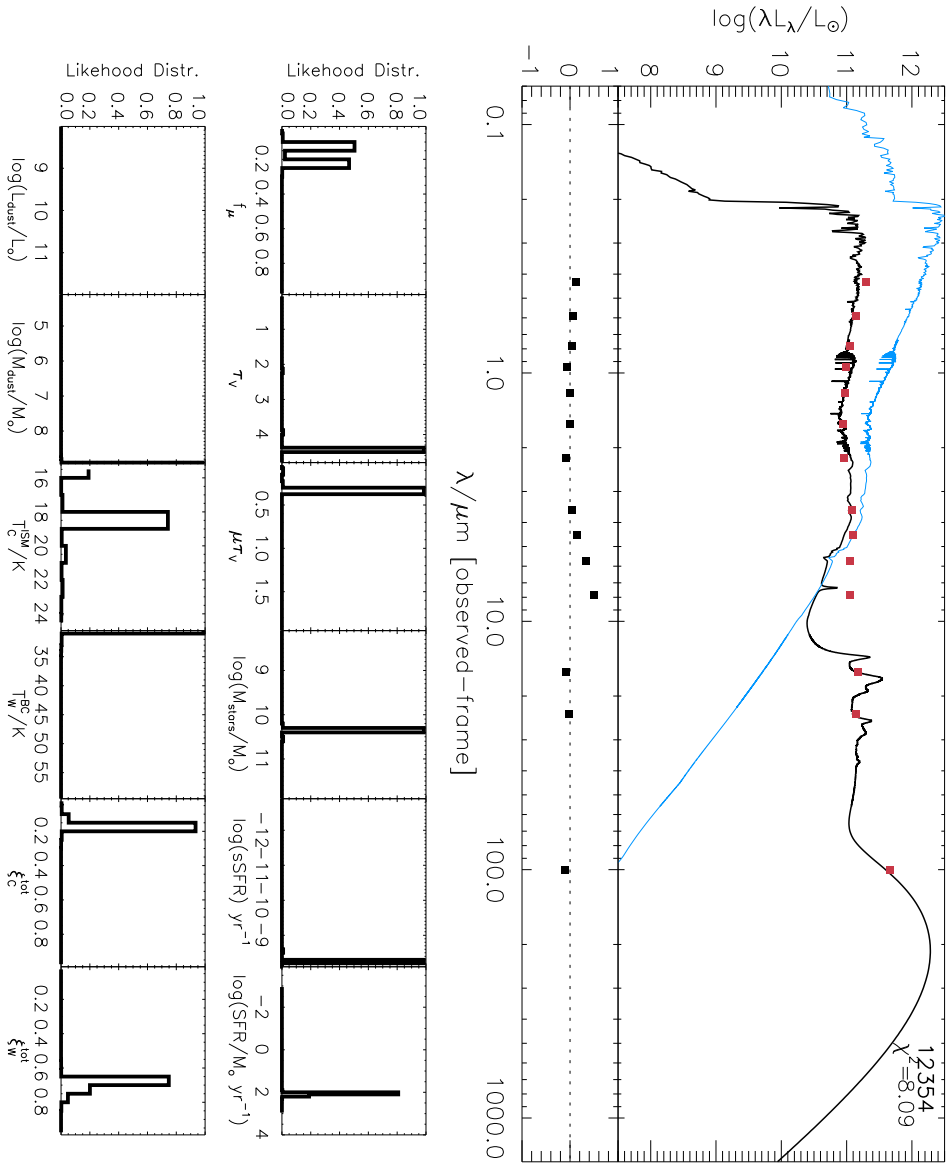

Figure 5.3: Spectral energy distribution of the object 12354. We can observe the luminosity excess in the near-IR and mid-IR, non fitted by the theoretical SED, which can arise from an AGN contribution.

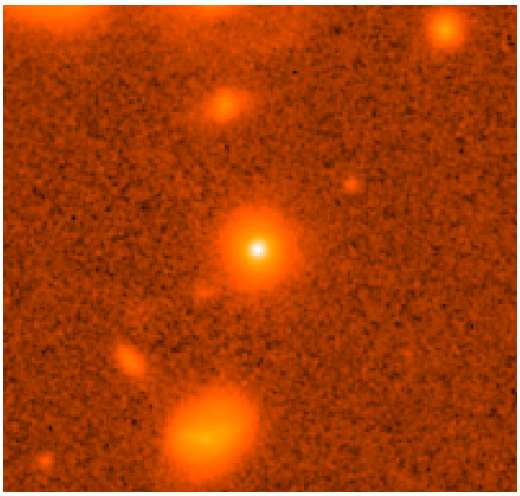

Figure 5.4: WFC3/F125W image of source 12354.The object shows a point source intense emission, as expected by an AGN.
The image has a scale of $0.06 arcsec/pixel$. North is up and East is left.

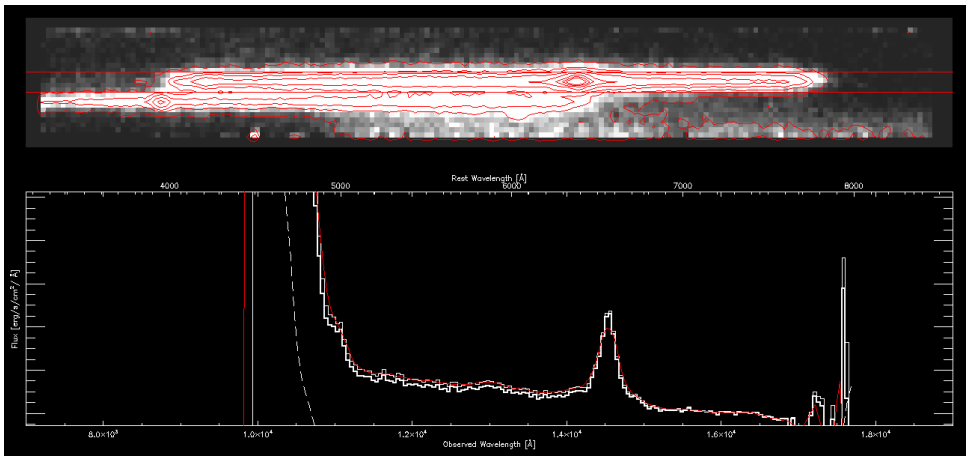

Figure 5.5: WFC3/G141 spectrum of source 12354. In the upper panel it is plotted the 2D spectrum, the bottom panel shows the extracted 1D spectrum. The spectrum is dominated by the Hα emission, that results intense and broadened.

Chapter 6

Extinction corrections

The impact of the dust on the spectrum of a galaxy can be evaluated from the cosmic background spectrum. The background light at 40 μm contains between the 50% and 70 % of the bolometric emission of galaxies integrated on redshift. This wavelength range is where it is re-emitted most of the stellar light absorbed by dust.
The far-IR emission at $8 - 120\mu$m measured by IRAS for nearby galaxies represents only the 25% of the bolometric output of these systems. However, when compared with the galaxy output in the UV, the energy in the IRAS bands represents between 1/2 and 2/3 of the total UV+far-IR emission in local galaxies. Regions of active star formation emit the bulk of their energy in the UV, owing the presence of young and massive stars, and the UV light reprocessed by dust is the principal contribute to the far-IR emission in the IRAS bands. Therefore one can conclude that between 1/2 and 2/3 of the star formation in the Local Universe is obscured by dust.
Applying the correction methods tested in the Local Universe also at high redshift, it was observed that the UV light of distant star forming galaxies can be obscured between 60% and 80%. This result has a strong impact on a lot of properties of the high redshift Universe, including the estimate of the star formation rate in galaxies. Moreover, the selective absorption of dust as a function of wavelength is the main reason for the discrepant results given by different SFR indicators.
Quantifying the impact of dust on the light emitted by the stellar component of galaxies allows us to improve our understanding of the evolution of star formation.

6.1 Classical treatment of the dust extinction

According to Calzetti et al. (2000)[5], the action of dust on starlight can be parameterized in a simple way in the wavelength range
$\lambda \in [0.12 - 2.2]\mu$m for starburst galaxies in the local Universe:

$$F_{obs}(\lambda) = F_{int}(\lambda)10^{-0.4A_\lambda} = F_{int}(\lambda)10^{-0.4E_{star}(B-V)k(\lambda)} \tag{6.1}$$

$$E_{star}(B-V) = (0.44 \pm 0.03)E_{neb}(B-V) \tag{6.2}$$

$$k(\lambda) = \begin{cases} 2.659(1.857 + \frac{1.040}{\lambda} + 4.05) & \lambda \in [0.63 - 2.20]\mu m \\ 2.659(2.156 + \frac{1.509}{\lambda} - \frac{0.198}{\lambda^2} + \frac{0.011}{\lambda^3}) + 4.05 & \lambda \in [0.12 - 0.63]\mu m \end{cases} \tag{6.3}$$

$$\beta = 1.9E_{neb}(B-V) + \beta_0 \tag{6.4}$$

$F_{obs}(\lambda)$ and $F_{int}(\lambda)$ are the dust-obscured and the intrinsic stellar continuum flux densities, respectively; A_λ is the dust obscuration suffered by the stellar continuum; $E_{star}(B-V)$ and $E_{neb}(B-V)$ are the color excess of the stellar continuum and of the nebular emission lines; $k(\lambda)$ is the starburst obscuration curve and β is the UV continuum slope measured between 0.125 μm and 0.26 μm, that is a sensitive indicator of both reddening and obscuration. The value of the intrinsic UV slope, β_0, depends slightly on assumptions on the star formation history of the starburst (e.g. β_0=-2.1 and -2.3 for constant star formation over 1 Gyr and over 100 Myr, respectively).
These equations are a simple and empirical recipe to apply dust corrections and give informations about the physical conditions of starbursts. Equation 6.1 implies that dust which obscures the starburst behaves as if it externally surrounds the regions of active star formation. The starburst environment is inhospitable to the dust, due to the high energy densities, to the shocks from SuperNovae explosions and to the possible gas outflows. However, equation 6.4 implies that the stars ionizing the gas are statistically well mixed with the stars producing the UV continuum, although equation 6.2 implies that the ionized gas suffers about

twice as much reddening as the stars.
A way out from this empasse is to assume that the ionized gas is more closely associated to the dust than the stars responsible for the UV emission. The ionizing stars may or may not be as dusty as the ionized gas, while the non-ionizing, UV-emitting stars will generally be less obscured than the gas as they live long enough to diffuse into regions of lower dust density.
The properties of dust in local galaxies were well studied mainly with three methods:

- The L_{IR}/L_{UV} (IRX) ratio, which probes dust attenuation using energy conservation since it is directly related to the UV continuum slope β (Meurer et al. (1999) [33])
- The analysis of the SED fitting or colors analysis
- A line of sight analysis using a luminous background object

The extinction in HII regions is directly computed from recombination lines ratios, often using the Balmer Decrement that is the ratio between the fluxes of Hα/Hβ lines. The intrinsic ratio can be determined starting from reasonable environmental parameters. Since the extinction is proportional to the wavelength, the comparison between the measured ratio and the intrinsic ratio with an extinction law allows to obtain a measure of the attenuation in the star forming regions.

6.2 Dust extinction in the high redshift Universe

The nature of dust in high redshift objects is less clear. Several works on dust in high redshift sources hare focused on the UV slope, although deviations from the Meurer et al IRX-β have been found for galaxy samples with different properties (e.g. Kong et al. (2004) [25]). Whitaker et al. (2014) [47] show that the curve of Meurer et al. for the relationship IRX-β derived in the local Universe, is valid only for the objects in their sample whit $z > 1.5$ and $\beta > 0.5$, so for the less obscured sources. Therefore, the use of UV slope to evaluate the attenuation on the continuum requires careful calibrations.
In addition indirect methods were examinated to evaluate the attenuation in the HII regions which are based on the infrared luminosity L_{IR} (Ibar et al. (2013) [18]) and comparison between SFR indicators (Wuyts et al. (2013) [48]). Direct measurements of dust attenuation towards

HII regions from the Balmer Decrement are very challenging at $z > 0.5$ because both Hα and Hβ are shifted to the less-accessible near-infrared window.

Current studies on dust properties in distant star forming galaxies leads to contrasting results:

- Erb et al. (2006) [13] , Reddy et al. (2010) [38] determine that the assumption of an extra extinction factor for HII regions as computed by Calzetti et al. (equation 6.2) leads to an overestimate of the $SFR_{H\alpha}$ relative to the SFR_{UV}
- Föster Schreiber et al. (2009) [14] require an extra extinction to conciliate the measurements of $A_{H\alpha}$ and $A_{V,star}$
- Yoshikawa et al. (2010) [49] found that high redshift objects are consistent with the local Universe comparing $A_{V,star}$ derived from the SED fitting and $A_{H\alpha}$ from the Balmer Decrement.
- Wuyts et al. (2013) [48] determine that the best agreement between $SFR_{H\alpha}$ and SFR_{IR+UV} can be obtained only adopting an extra extinction factor.
- Kashino et al. (2013) [19] use a comparison between star formation indicators and an analysis of the Balmer Decrement on a relatively large sample at $1.4 < z < 1.7$ and derive that there is necessity of an extra extinction factor, slightly lower than the conversion factor derived in the local Universe
- Price et al. (2013) [37] use the Balmer Decrement analysis on stacked spectra acquired from the 3D-HST survey at $z \sim 1.5$ to found a nebular extinction $A_{H\alpha} \simeq 1.81 A_{V,star}$, a value lower than the factor 2.27 of Calzetti et al. computed in the low redshift Universe.

The result of Price et al. and the comparison with the works of Wuyts, Calzetti and Kashino are shown in Figure 6.1: it is inconsistent with the assumption of no extra extinction in the star forming regions; it is consistent with Wuyts et al.; it agrees with the Kashino's analysis on the SFR indicators; it is in disagreement with the analysis of Kashino on the Balmer Decrement.
The contrasting results listed here are not surprising, given the different and indirect methods used and/or the small and often biased samples of most of these studies. To clarify dust properties direct measurements of a statistical sample are required.

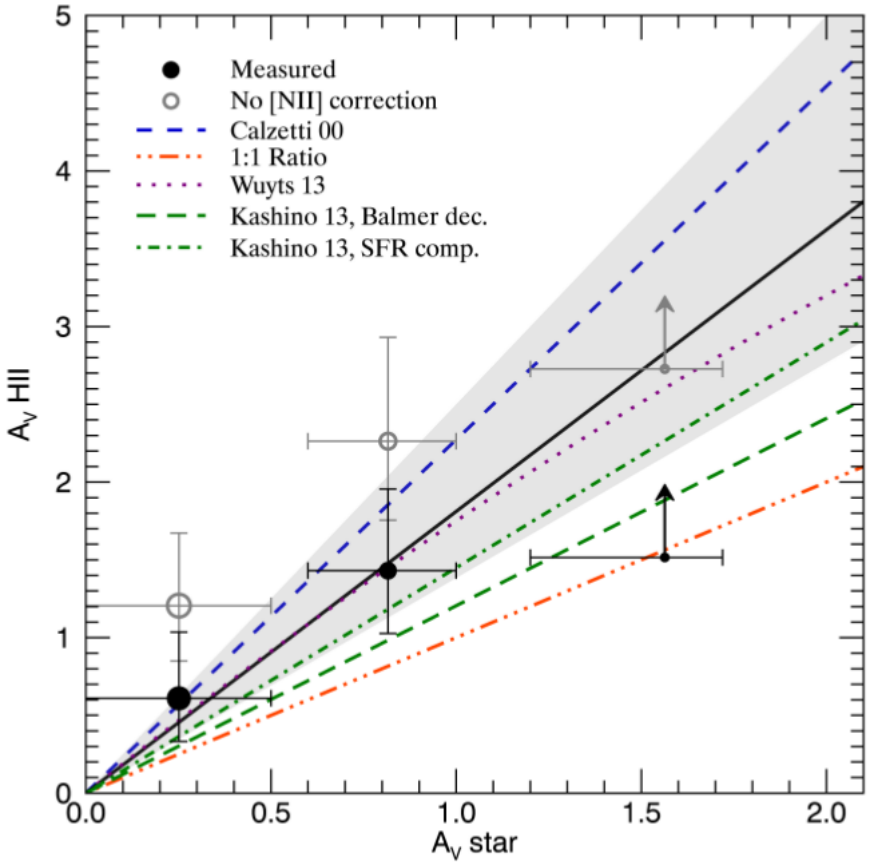

Figure 6.1: $A_{V,star}$ vs. $A_{V,HII}$ measured from the spectra stacked in bins of $A_{V,star}$. The black circles show the measured $A_{V,HII}$ using the Balmer decrement (Hα/Hβ), while the grey open circles show the value of $A_{V,HII}$ if the blended Hα line was not corrected to remove the [NII] flux. The blue dashed line shows ratio of $A_{V,HII}$ to $A_{V,star}$ from Calzetti et al. (2000). The orange dash-dot-dot line shows the ratio of $A_{V,HII}$ to $A_{V,star}$ assuming no extra dust extinction towards emission line regions. The black line shows the best-fit line to the black data points, which has a slope of 1.81. The fit error is shown with the shaded grey region. This indicates there is extra extinction towards emission line regions, but not as much as Calzetti et al. (2000) finds necessary for low redshift galaxies. The best-fit line is consistent with the findings of Wuyts et al. (2013), shown with the purple dotted line. The green long dash and green dash-dot lines show the relations found by Kashino et al. (2013). From Price et al. (2013) [37]

In general, the results are consistent with a two components model which assumes a diffuse but possibly clumpy component of the ISM that affects both the oldest stellar populations and the star forming regions, and a optically thick component associated to the birth clouds which affects only the youngest stars.
The validity of this model seems to be confirmed also by the trend of the specific SFR ($sSFR$=SFR/M_*) with respect to the extra extinction

factor $\Delta A_V = A_{H\alpha} - A_{V,star}$: increasing the sSFR, the extra extinction factor ΔA_V is decreasing. For higher values of sSFR the continuum is dominated by the most massive stars, which are located in the birth cloud and this implies $A_{H\alpha} \sim A_{V,star}$. On the contrary, if the sSFR is lower, the contribution of the most massive stars to the galaxy continuum is lower so most of the luminosity of the continuum comes from the oldest stars, attenuated only by the diffuse component of dust: the results is that $A_{H\alpha}$ is larger than $A_{V,star}$.
The model is pictured in figure 6.2 of Price et al.

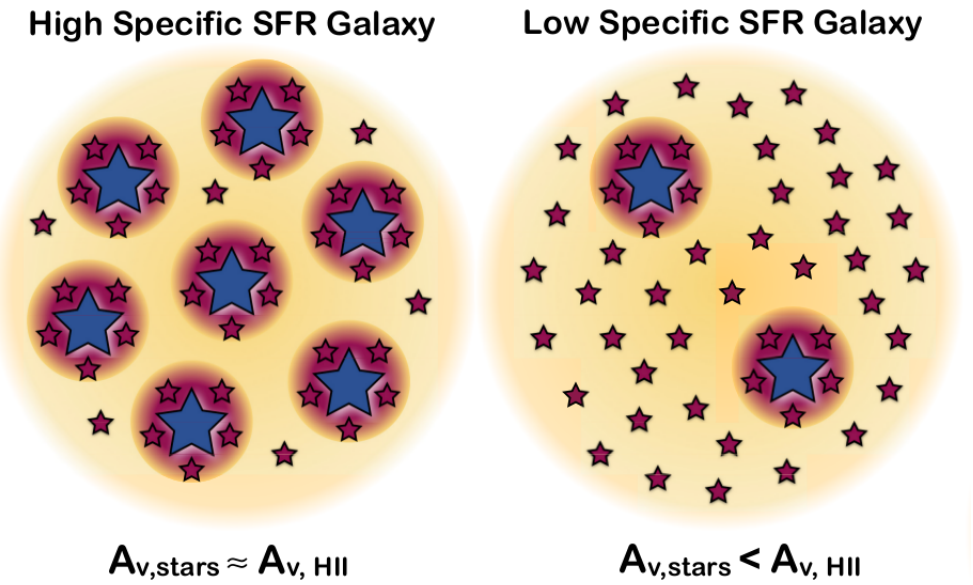

Figure 6.2: Illustration of the two-components dust model in galaxies with high (left panel) and low (right panel) specific SFRs. The yellow regions indicate the diffuse dust component in the ISM. The red regions indicate the optically thick dust component associated with the short-lived stellar birth clouds. The large blue stars show the young, massive stars which mostly are found in the birth clouds. The small red stars show the less massive stars (both young and old), which are found both within the birth clouds and elsewhere. For galaxies with higher specific SFRs, we expect the continuum light to be dominated by the young, massive stars in the birth clouds, so both the continuum and emission lines are attenuated by both dust components. Galaxies with lower specific SFRs would have a higher contribution to the continuum emission from less massive stars, which generally reside outside the birth clouds and are only attenuated by the diffuse dust component, while the emission lines are still attenuated by both dust components. Thus this leads to larger differences between $A_{V,star}$ and $A_{V,HII}$.
From Price et al. (2013) [37].

In this work we adopt some of the methods listed above to correct the Hα fluxes for dust extinction and we evaluate the best extinction factor for our sample by comparing the $SFR_{H\alpha}$ with SFR_{IR+UV}, which we assume to be the best estimate for the star formation rate for our sample.

6.3 Extinction from f-factors

Following the approach of Kashino et al. we derive the color excess on the Hα line from the color excess on the stellar continuum and a Calzetti extinction law, by applying the equations:

$$E_{neb}(B-V) = \frac{E_{star}(B-V)}{f} \tag{6.5}$$

$$F_{int}(H\alpha) = F_{obs}(H\alpha)10^{0.4\times 3.327 E_{neb}(B-V)} \tag{6.6}$$

$$A_{H\alpha} = 3.327 \times E_{neb}(B-V) \tag{6.7}$$

We evaluate $E_{neb}(B-V)$ for four different values of the conversion factor f:

- f=0.44 is the factor computed by Calzetti et al. for local star forming galaxies;
- f=0.69 is derived by Kashino et al. from a comparison between SFR indicators;
- f=0.83 is determined by Kashino et al. from an analysis of the Balmer Decrement;
- f=0.76 is the mean value between the two previous values of Kashino et al.

The color excess on the stellar continuum $E_{star}(B-V) = (B-V)_{obs} - (B-V)_{int}$ is derived from the SED fitting. The procedure is summarized in figure 6.3: the extinguished SED (black line) and the stellar SED unextinguished (red line) are convolved with the filters in the B and V bands to obtain the observed color $(B-V)_{obs}$ and the intrinsic color $(B-V)_{int}$.

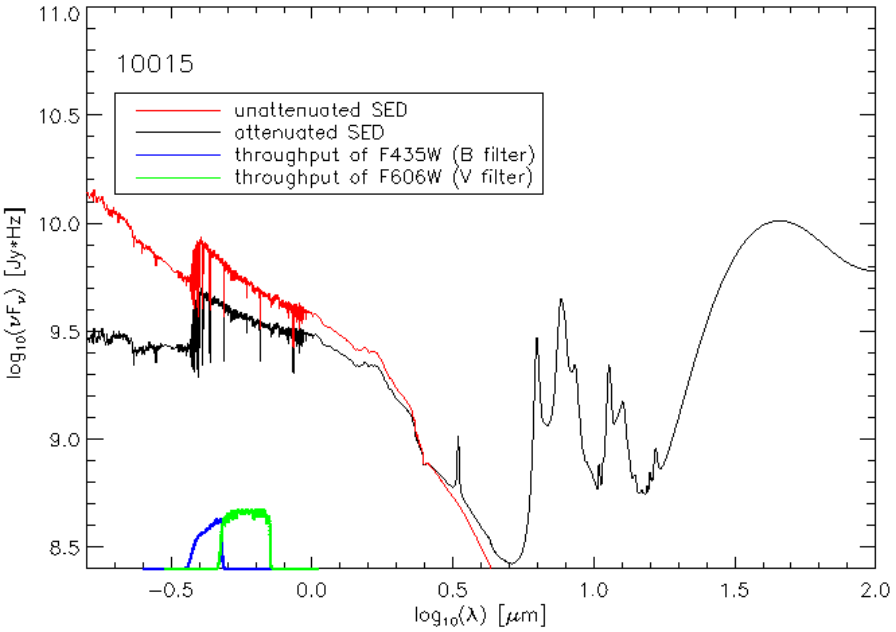

Figure 6.3: Computation of the color excess on the stellar continuum, $E_{star}(B-V) = (B-V)_{obs} - (B-V)_{int}$ for the source 10015.
The black line is the extinguished SED computed with MAGPHYS and the red line is the unattenuated stellar SED. The two curves are convolved with the ACS filters F435W ($\lambda_{eff} = 0.4297\mu$m) and F606W ($\lambda_{eff} = 0.5907\mu$m) to obtain the colors $(B-V)_{obs}$ and $(B-V)_{int}$.

6.4 Extinction from the stellar masses

Still following the analysis of Kashino et al., we consider an independent (but less accurate) method to derive the attenuation in the nebular lines $A_{H\alpha}$, from M_* with the Kashino's relationship:

$$A_{H\alpha} = (0.72 \pm 0.04) + (1.38 \pm 0.05) log \left[\frac{M_*}{10^{10} M_\odot} \right] \qquad (6.8)$$

The stellar masses M_* are derived from the SED fitting. Equation 6.8 is a best-fit relation to the Kashino's sample, valid for a particular set of normal star forming galaxies (selected with the BzK color criterion) at $z \sim 1.5$.

6.5 Extinction from the UV slope

We derive the extinction from the relationship of Meurer et al. (1999) [33] which links the ratio between the total infrared luminosity and the UV luminosity at 1600 Å F_{IR}/F_{1600} (IRX), to the slope of the UV spectrum β:

$$A_{1600} = 4.43 + 1.99\beta \tag{6.9}$$

$$A_{H\alpha} = 3.326A_{1600}/9.97 \tag{6.10}$$

The UV slope is derived from a linear fit to the model best-fit SED in the wavelength range $\lambda \in [1250 - 2600]$Å.
Figure 6.4 shows the trend of the IRX ratio as a function of the slope of the UV spectrum β. The monochromatic luminosity at 1600Å F_{1600} and the total infrared luminosity F_{IR} are derived from the SED fitting. The green line represents the relationship of Meurer et al. derived from calibrations on a sample of local starburst galaxies:

$$IRX_{1600} = 10^{0.4A_{1600}} - 1 + 0.076 \tag{6.11}$$

while the blue line is the relationship of Kong et al. 2004 [25], evaluated on a sample of local galaxies that spans a wide range of star formation activities:

$$IRX_{1600} = 10^{2.1+0.85\beta} - 0.95 \tag{6.12}$$

The galaxies of our sample at lower redshift ($z < 1$, black filled circles) follow mainly the Meurer's law, while the more distant objects ($z > 1$, red squares) better agree with the Kong relationship.

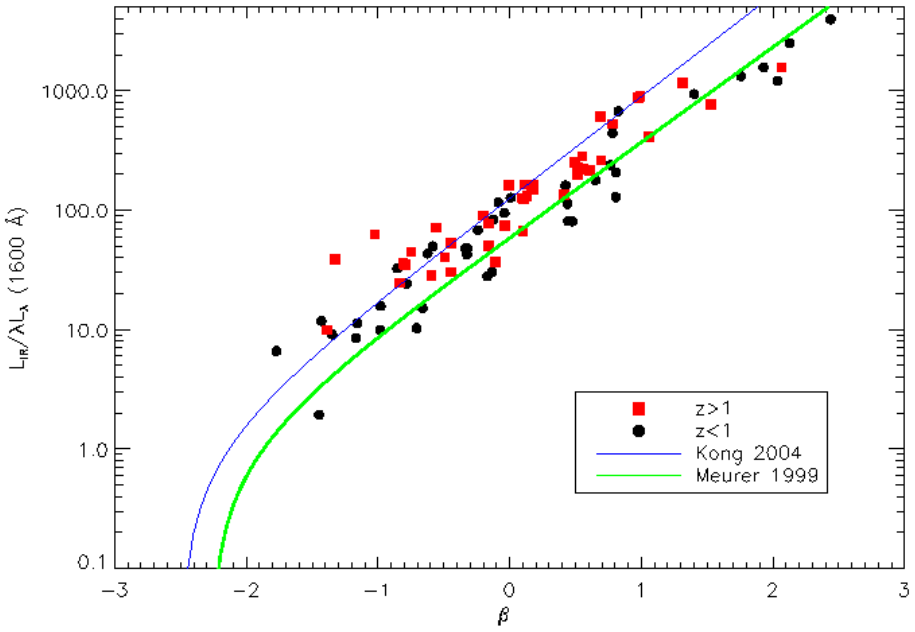

Figure 6.4: Ratio of far-IR to UV flux at 1600Å compared to the UV spectral slope β for 3D-HST sources. The green line is the relationship between IRX_{1600} and A_{1600} as derived by Meurer et al. (equation 6.11) from calibrations on a sample of local starburst galaxies. The blue line is the relationship IRX_{1600}-A_{1600} determined by Kong et al. (equation 6.12) on a sample of 115 nearby, non-Seyfert galaxies spanning a wide range of star formation activities, from starburst to nearly dormant.
The black dots are the 3D-HST galaxies with $z < 1$, while the red squares are the sourecs with $z > 1$.

6.6 Extinction from the IR luminosity

We also estimate the extinction on the Hα line from the bolometric infrared luminosity L_{IR}, using the formalism of Ibar et al. 2013 [18]. The authors apply the prescription of Kennicutt et al. (2009) [22] to evaluate the dust correction from the formulas:

$$L_{corr}(H\alpha) = L_{obs}(H\alpha) + a_\lambda L_{IR} \tag{6.13}$$

$$A_{H\alpha} = 2.5log\left[1 + \frac{a_\lambda L_{IR}}{L_{obs}(H\alpha)}\right] \tag{6.14}$$

where:

$$a_\lambda = 0.0025 \pm 0.0006 \tag{6.15}$$

The dust extinction corrections derived with the four methods described in this chapter will be applied to the observed Hα fluxes for our sample. The different corrections will be used to compute SFR from the Hα luminosity, to be compared with SFR from the $IR + UV$ luminosity.
The results of this exercise are presented in the next chapter.

Chapter 7

Comparison between SFR indicators

To evaluate the best correction factor for dust extinction towards the HII regions in our sample, we compare the SFR measurements derived from the Hα fluxes with the estimate of the SFR from the infrared+ultraviolet luminosity.

7.1 SFR from Hα compared to SFR from far-IR

We correct the Hα flux for the aperture using the scale factor F_{spec}/F_{SED} derived from the SED scaling (for details see section 4.3.2). We have also to correct the line flux for the [NII] contribution. The G141 resolution is not sufficient to split the two emission lines, so the two lines are blended. As done by Wuyts et al. (2013), which examined 3D-HST spectra in the same redshift range, we apply a simple downscaling of the observed emission line flux by a factor 1.2. In reality, the [NII]/Hα ratios may vary between galaxies but, restricting the above spectroscopic samples to the same redshift range as adopted in this work, the scatter in [NII]/Hα is substantial compared to any systematic trend, if present, with galaxy mass above $log(M_*) = 10$. Furthermore, the [NII]/Hα gradients derived from observations realized with adaptive optics are typically shallow. We conclude that an higher order correction than the uniform scaling factor we apply is not justified by present data.

We compute the star formation rates from the Hα luminosities using the equation of Kennicutt 1998 [20], illustrated in the first chapter (equation 1.3) and reported here for convenience:

$$SFR_{H\alpha}[M_{\odot}/yr] = 7.9 \times 10^{-42} L_{H\alpha}[erg/s] \tag{7.1}$$

We remind also that this relationship is calibrated for a Salpeter IMF.

To include the unobscured SFR not traced by the IR, we add the SFR derived from the UV, following the formalism of Rodighiero et al. 2010 [39]:

$$SFR_{IR+UV}[M_{\odot}/yr] = 1.8 \times 10^{-10} L_{bol}[L_{\odot}] \tag{7.2}$$

where:

$$L_{bol} = 2.2 L_{UV} + L_{IR}[L_{\odot}] \tag{7.3}$$

L_{IR} was derived from the best-fit SEDs in the $[8 - 1000]\mu$m rest-frame range while the rest-frame UV luminosity (which accounts for the contribution of young unobscured stars), uncorrected for extinction, derived again from the SED fitting, is $L_{UV} = 1.5 \times L(2700$ Å$)$. We consider the measure of SFR_{IR+UV} as our best estimate of the star formation rate.
We report in Figure 7.1 the comparison between SFR_{IR+UV} and $SFR_{H\alpha}$ with the Hα luminosities uncorrected for dust extinction, to stress the necessity of adopting a dust correction with an extra extinction factor for the HII regions, mapped by the Hα line. The black dots are the $SFR_{H\alpha}$ measurements derived without correcting the Hα fluxes for dust extinction: the absence of a dust correction leads to an evident underestimate of the star formation rate. The green dots show the $SFR_{H\alpha}$ corrected for dust extinction without considering an extra extinction factor between the color excess on the continuum $E_{star}(B-V)$ and the color excess on the nebular lines $E_{neb}(B-V)$: also this correction is not sufficient to report in agreement the two SFR indicators and the $SFR_{H\alpha}$ results still underestimated.

In the following pages we report the comparison between the two star formation indicators SFR_{IR+UV} and $SFR_{H\alpha}$ by varying the dust correction for measurements of Hα fluxes. In each plot, the black dots represent the sources with redshift lower than 1 while the red squares correspond to the objects with $z > 1$. The blue solid line in all the figures stands for the 1:1 correlation line.

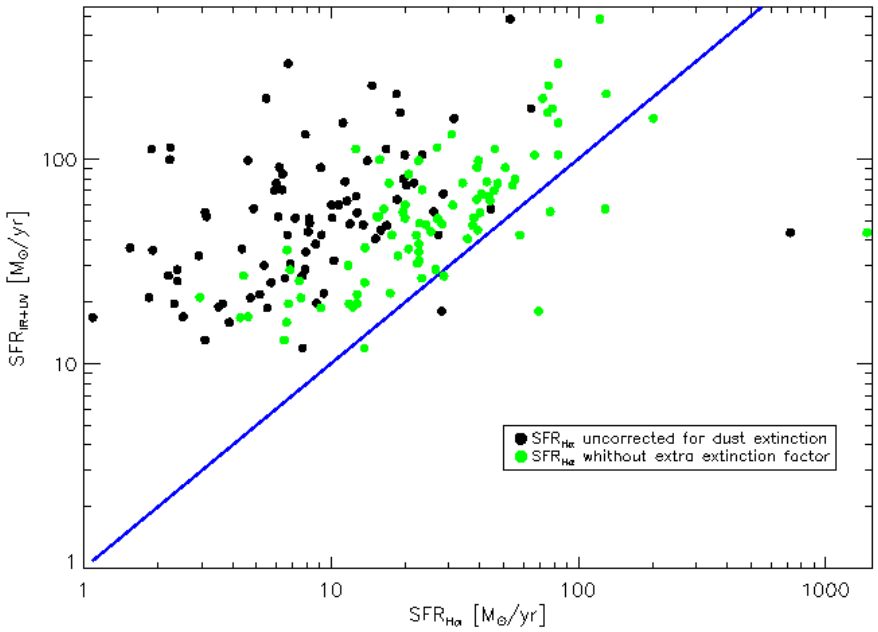

Figure 7.1: Comparison between SFR_{IR+UV} and $SFR_{H\alpha}$ in two cases: the black dots show the $SFR_{H\alpha}$ measurements in absence of dust correction; the green dots are the $SFR_{H\alpha}$ with the Hα fluxes corrected for dust absorption in absence of an extra extinction factor for the emission lines.
This plot stress about the necessity of adopting an extra extinction factor to correct Hα line fluxes for dust absorption since the absence of dust correction leads to a significant underestimate of the derived $SFR_{H\alpha}$ in comparison between the SFR_{IR+UV} that reasonably accounts for the total star formation of a galaxy.

Figure 7.2 shows the comparison between SFR_{IR+UV} and $SFR_{H\alpha}$ with the Hα fluxes corrected for dust extinction using the equations 6.5 and 6.6. In the first panel the dust correction is applied using an f-factor of 0.44, as Calzetti et al.: this heads to an overestimate of the $SFR_{H\alpha}$. The remaining panels show the dust correction with the f-factor values reported by Kashino et al.: these values of f lead to a better agreement between SFR indicators and, in particular, the factor f=0.69 derived from the comparison between SFR indicators gives the smallest scatter relative to the 1:1 line.

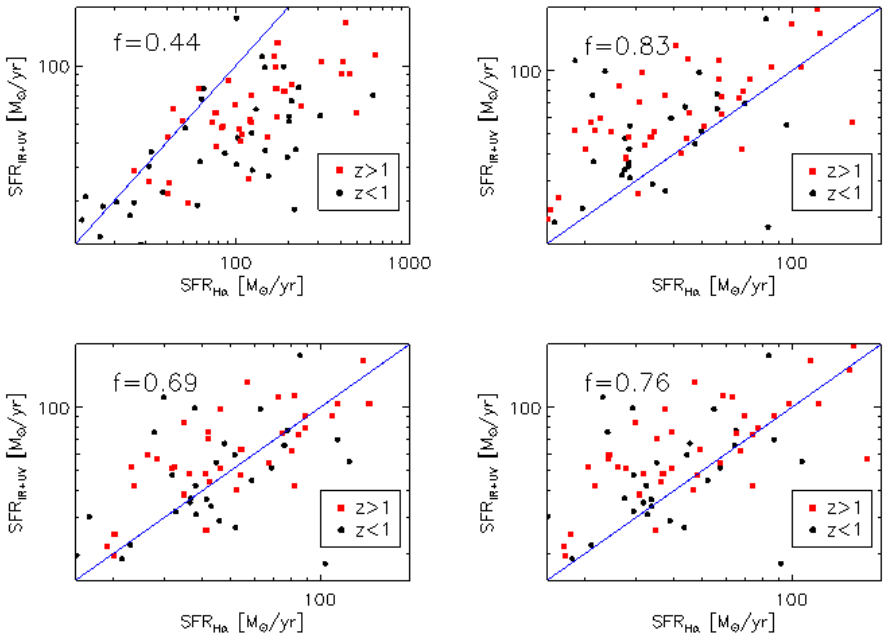

Figure 7.2: Comparison between SFR_{IR+UV} and $SFR_{H\alpha}$ on varying the conversion factor f between colour excess on nebular lines and on stellar continuum (equations 6.5 and 6.6). The black dots are the sources with $z < 1$, the red squares are the objects with $z > 1$ and the blue line is the 1:1 correlation line.
The Hα luminosities derived from 3D-HST spectra and here used to compute $SFR_{H\alpha}$ measurements are corrected for dust extinction using the standard approach of Calzetti [5] (first panel, f=0.44) and the methodology of Kashino [19] (others panels, f=0.69 , 0.83, 0.76). A standard correction factor of f=0.44 yields to values of $SFR_{H\alpha}$ systematically higher than SFR_{IR+UV} . Using the prescriptions of Kashino we found an higher degree of correlation. The best trend is obtained applying a conversion factor of 0.69.

Figure 7.3 reports the correlation between $SFR_{H\alpha}$ and SFR_{IR+UV} with the dust attenuation $A_{H\alpha}$ derived from the stellar masses M_* (Kashino's equation 6.8). The stellar masses M_* are derived from the SED fitting and are valid for a Chabrier IMF while the equation 6.8 is valid for a Salpeter IMF: to convert our estimate of M_* we use a constant factor of 1.7, since the stellar masses evaluated for a Salpeter IMF are larger than M_* computed for a Chabrier IMF.

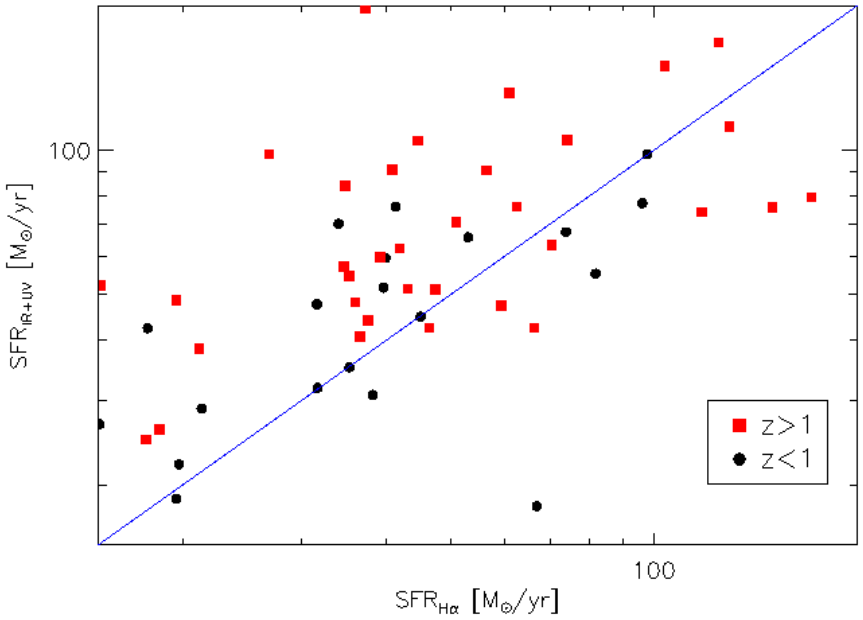

Figure 7.3: Comparison between $SFR_{H\alpha}$ and SFR_{IR+UV}. In this case the dust correction is applied determining $A_{H\alpha}$ from the relationship 6.8 of Kashino et al. This correction for dust extinction is better than the standard correction but leads to a broad scatter of data points. We point out that the equation 6.8 is a best-fit estimate on a sample with different ranges of redshift, stellar masses and SFR.

In Figure 7.4 we compare the measurements of the SFRs using a correction for dust extinction derived from the slope of the UV spectrum β in the wavelength range $\lambda \in [1250 - 2600]$Å, adopting the prescription of Meurer et al. (equation 6.10). Using the UV slope to evaluate the dust attenuation, we obtain a good agreement between SFR indicators even if SFR_{IR+UV} is still a factor ~ 1.4 larger than $SFR_{H\alpha}$, as shown in Table 7.1. However we have to point out that the slope β was evaluated throughout a linear fit to the theoretical SED (we report to the 5^{th} chapter for the description of the SED fitting procedure), lacking the photometric covering the wavelength rest-frame range of interest , so the trend can be an induced, model dependent, effect. We highlight that for 31 objects in our sample it lacks the U data at 3460 Å in the MUSIC catalog.

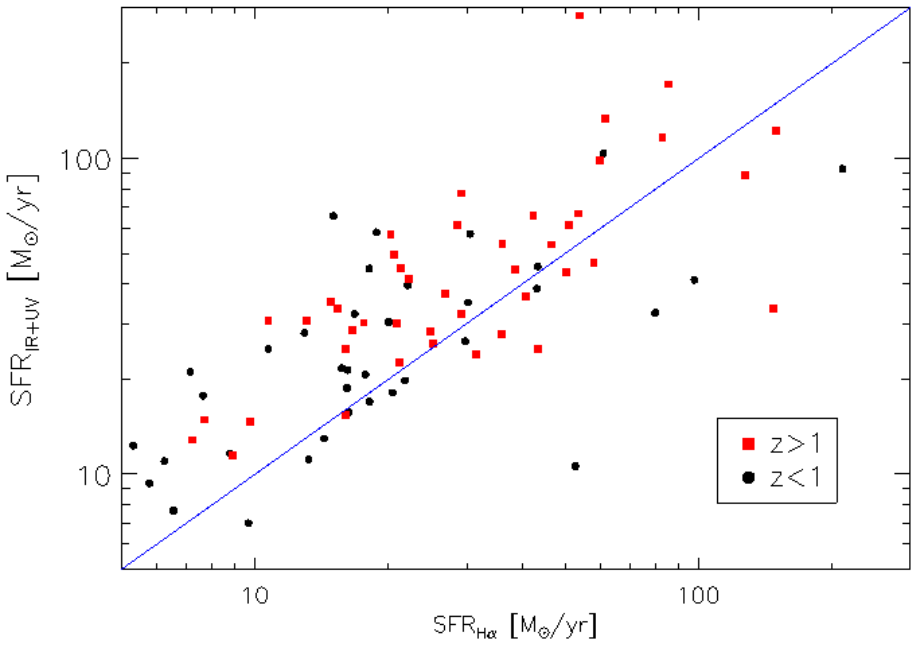

Figure 7.4: Comparison between $SFR_{H\alpha}$ and SFR_{IR+UV}. The attenuation by dust $A_{H\alpha}$ here is evaluated from the UV spectral slope β, as prescribed in Meurer et al.. This correction leads to a suitable correlation between SFR indicators but we highlight that the slope β is computed from a linear fit to the theoretical SEDs, because of the lack of the photometric coverage, so the results are model-dependent. A more reliable estimate of the spectral slope can be obtained fitting the observed photometry.

Figure 7.5 shows the comparison between the two SFR measurements in the case of extinction derived from the infrared luminosity (equations 6.13 and 6.14), as done in Ibar et al. 2013. The relationship between the two star formation rate measurements shows an offset of a factor ~ 1.7, with the $SFR_{H\alpha}$ systematically underestimated in respect to the SFR_{IR+UV}, even if the scatter of the data points is the lowest of all the adopted methods for dust correction. This offset seems related to the different properties of galaxies examined in the samples. The Kennicutt samples cover a restricted range in attenuation and corresponding observed ratio $L_{IR}/L_{H\alpha}$, which encompasses all normal galaxies in the present-day Universe and most star-forming galaxies out to redshifts $z \sim 1$ but it does not includes the most luminous star-forming galaxies found at high redshift as galaxies in our sample. The presence of this offset is reminded by Kennicutt.
With reference to the reduced scatter of this plot, we stress about the point that the two measurements here compared are not independent. The infrared luminosity L_{IR} from which we evaluate the SRF_{IR+UV} is here used also to correct the Hα flux for dust extinction: to verify if this

can be a suitable recipe to evaluate the dust attenuation, we need to compare the $SFR_{H\alpha}$ to a fully independent quantity. Both the presence of the offset (whose nature and precise magnitude are at the moment not completely clarified) and the induced high level of correlation between SFR measurements, lead us to not consider this method as a valid tracer of dust extinction. We present in any case the comparison for completeness.

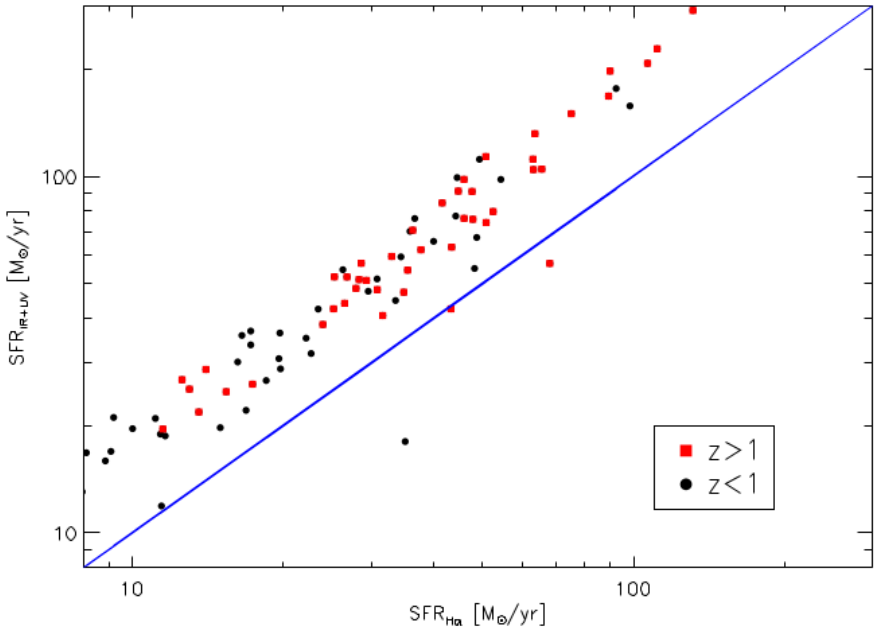

Figure 7.5: Comparison between $SFR_{H\alpha}$ and SFR_{IR+UV}. In this case the intrinsic $H\alpha$ luminosity is derived from the observed $L_{H\alpha}$ and the bolometric L_{IR}, applying the equation of Kennicutt [22]. The $SFR_{H\alpha}$ is then computed using the Kennicutt98, as Ibar et al.[18].
The plot shows a tight relationship between SFR indicators with an offset of a factor about 2, as expected for systems that lie outside of the bounds of the calibration of Kennicutt et al. The calibration in fact does not encompass the star forming galaxies at high redshift. This result is consistent with Ibar et al..
The reduced scatter here observed is due to the fact that the two compared quantities are not fully independent: the infrared luminosities are used to estimate the SFR_{IR+UV} and also to correct the $H\alpha$ luminosities for dust extinction.

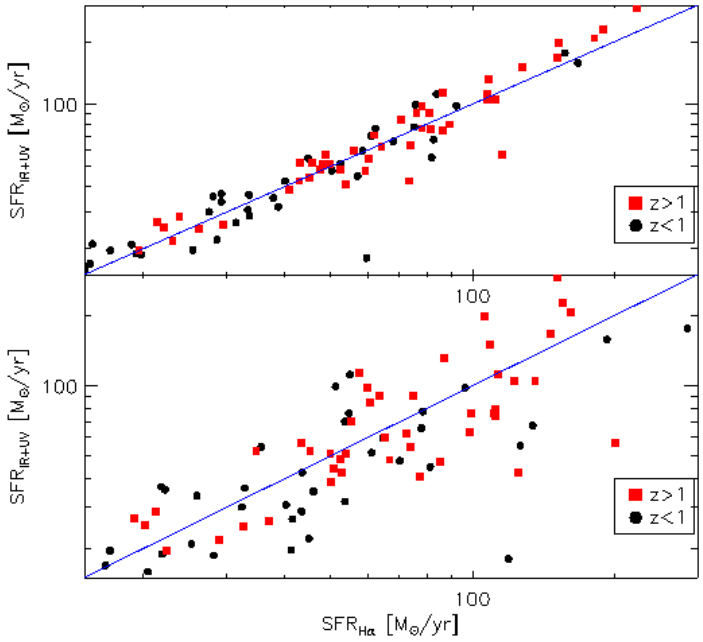

Figure 7.6: Comparison between $SFR_{H\alpha}$ and SFR_{IR+UV} adopting the correction for dust extinction of Kennicutt (2009).
Upper panel: In this case we apply a factor of 1.7 to the intrinsic Hα luminosity $L_{corr}(H\alpha) = 1.7 \times (L_{obs}(H\alpha) + a_\lambda L_{IR})$. The presence of this factor removes the offset between the two measurements, seen in figure 7.5.
Lower panel: In this case we apply a factor of 4 to the observed Hα luminosity $L_{corr}(H\alpha) = 4 \times L_{obs}(H\alpha) + a_\lambda L_{IR}$. The offset is again removed but the data-points scatter is increased.

We include in Figure 7.6 a "test plot" where we compare again the SFR_{IR+UV} and the $SFR_{H\alpha}$ with a correction for dust extinction from Kennicutt (2009).
The upper part of Figure 7.6 shows the case in which the intrinsic Hα luminosity is derived from the quantity $1.7 \times (L_{obs}(H\alpha) + a_\lambda L_{IR})$: the factor 1.7 reconciles the two SFR estimates.
In the lower part of Figure 7.6 we modify only the value of $L_{obs}(H\alpha)$, multiplying it for a factor 4: the offset is removed but it is also increased the scatter of data-points.
We can conclude that, following the formalism of Kennicutt, it is necessary to increase the weight of both $L_{obs}(H\alpha)$ and L_{IR} in the computation of the correction for dust extinction to derive the intrinsic Hα luminosity for our sample.

The presence of the offset between the two SFR measurements was also found by Ibar et al. (2013) [18]. These authors work on a sample of Hα emitters galaxies at $z \sim 1.47$, which fulfill the applicability conditions of

the recipes of Kennicutt (2009) to derive the extinction from L_{IR}. The authors use a stacking PACS to derive the mean values of L_{IR}, so they do not cut the sample to a far-IR selection. Ibar et al. founds that the median ratio $[SFR_{FIR(K98)}/SFR_{H\alpha+FIR(K09)}] = 1.37$ and argue that if the dominant component is the far-IR (as probably in our PEP-3DHST sample) the discrepancy between $SFR_{FIR(K98)}$ and $SFR_{H\alpha+FIR(K09)}$ is increasing. The ratio tend to 2.27 in the extreme case where the line is completely obscured ($L_{obs}(H\alpha) = 0$), according to Kennicutt. The authors suggest a recalibration of the $SFR_{H\alpha}$ that takes into account the energetic balance between $SFR_{H\alpha,obs}$ and $SFR_{H\alpha+far-IR}$ to include the effect of dust extinction, using $SFR_{H\alpha,obs}/SFR_{H\alpha+far-IR}$ vs $mag_{3.6\mu m}$ since this ratio defines the dominant component of the SFR. A similar recalibration for our sample will be considered in a future work.

As a final exercise, we propose an alternative SFR estimator which combines the observed Hα luminosity uncorrected for dust extinction and the total infrared luminosity, that we express through the following equation:

$$SFR_{H\alpha,obs+IR} = 7.9 \times 10^{-42} L_{H\alpha,obs}[erg/s] + 1.8 \times 10^{-10} L_{IR}[L_{\odot}] \quad (7.4)$$

We compare this estimate of the SFR with the SFR_{IR+UV} (upper panel of Figure 7.7) and the $SFR_{H\alpha}$ corrected with the dust extinction law of Kennicutt (2009) 6.13 (lower panel of Figure 7.7). The comparison between $SFR_{H\alpha,obs+IR}$ and SFR_{IR+UV} yields to a good correlation, with a very low scatter of data-points ($\sigma(SFR_{IR+UV}/SFR_{H\alpha,obs+IR}) \sim 0.01$) and an offset of $SFR_{IR+UV}/SFR_{H\alpha,obs+IR} \sim 0.90$. By comparing $SFR_{H\alpha,obs+IR}$ and $SFR_{H\alpha}$ we obtain an offset $SFR_{H\alpha}/SFR_{H\alpha,obs+IR} \sim 0.52$ and a scatter $\sigma(SFR_{H\alpha}/SFR_{H\alpha,obs+IR}) \sim 0.05$.
We conclude again that the dust correction of Kennicutt 6.13 underestimates the contribution of $L_{H\alpha}$ and that a recalibration of the relationships 6.13 and 6.14 is required.

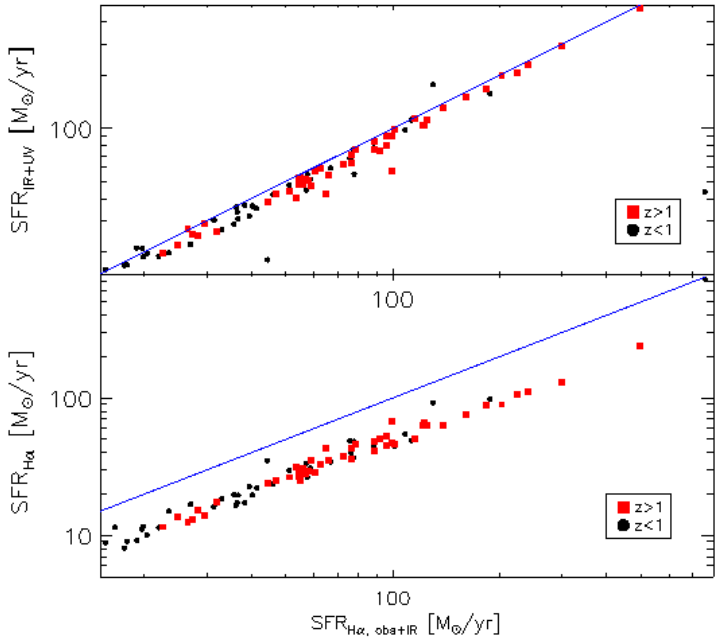

Figure 7.7: *Upper panel:* The x-axis is the SFR computed from the observed Hα luminosity (uncorrected for dust extinction) and the total infrared luminosity (equation 7.4). The y-axis is the SFR computed from the total infrared luminosity and the UV luminosity (i.e. our best estimate of the SFR, as discussed in the Thesis).
Lower panel: The $SFR_{H\alpha,obs+IR}$ is compared to the $SFR_{H\alpha}$ computed from the Hα luminosity corrected for dust extinction using the equation 6.13 of Kennicutt (2009).

7.2 The Main Sequence of star-forming galaxies at $z \sim 1$

The star-forming galaxies follow a tight relationship between M_* and SFR and define a main sequence (MS) recognized both in the local and in the high redshift Universe (Peng et al. (2010) [34]; Elbaz et al. (2007) [12]; Daddi et al. (2007) [9]; Rodighiero et al. (2010) [39]).
The slope and the normalization of this relationship can differ substantially depending on sample selection and the procedures for measuring M_* and SFR (Rodighiero et al. (2014) [40]).
It is known the existence of the "outliers" to this MS, defined as galaxies with extremely higher sSFR in respect to the main sequence galaxies. Outliers are objects where the star formation was boosted by some events, possibly a major merger. Main Sequence galaxies and outliers objects seem to be in different star formation regimes: a quasi-steady state, long lasting mode for the first kind of systems and a starburst mode in major mergers or in the densest star-forming regions.
It is so fundamental to define the outliers in our sample. To evaluate the number of starburst sources, we plot the relationship M_* versus SFR_{IR+UV} marking the MS at redshift $z \sim 1$ (Elbaz et al. 2007 [12]) as defined by the equation:

$$SFR[M_\odot/yr] = 7.2 \left(\frac{1.7 M_*}{10^{10} M_\odot} \right)^{0.9} \tag{7.5}$$

and the limit of outliers above $4 \times MS$. The plot is reported in figure 7.8. The MS is indicated with the green line while the $4 \times MS$ limit is shown with the blue line. We can observe that the lower redshift sources (black dots) occupy the lower part of the plot, whereas the more distant galaxies (red squares) lie in the higher part of the sequence.
Generally our data sample the main sequence and only a limited number of sources (5 out of 87 objects) are above the $4 \times MS$ limit and can be classified as outliers. Therefore, removing these objects from the analysis is not crucial for our results.
We underline that the galaxies in our sample seem to not follow the Elbaz relationship for the Main Sequence. We remind that this behavior is related to the selection criterion adopted for our sample, since our galaxies show quite high values of far-IR luminosity. As extensively discussed in the paper of Rodighiero et al. (2014) [40], the sample selection criterion affects both the slope and the normalization of the MS. In particular, selecting galaxies in a passband that is directly sensitive to the

SFR (such as the far-IR) automatically induces a Malmquist bias in favor of low-mass galaxies with above average SFRs, thus flattening the resulting $SFR - M_*$. This effect is clearly seen in Herschel FIR-selected samples, as our sample, where formally the slope of the relationship is $\simeq 1$ but where only a tiny fraction of galaxies are detected at low stellar masses.

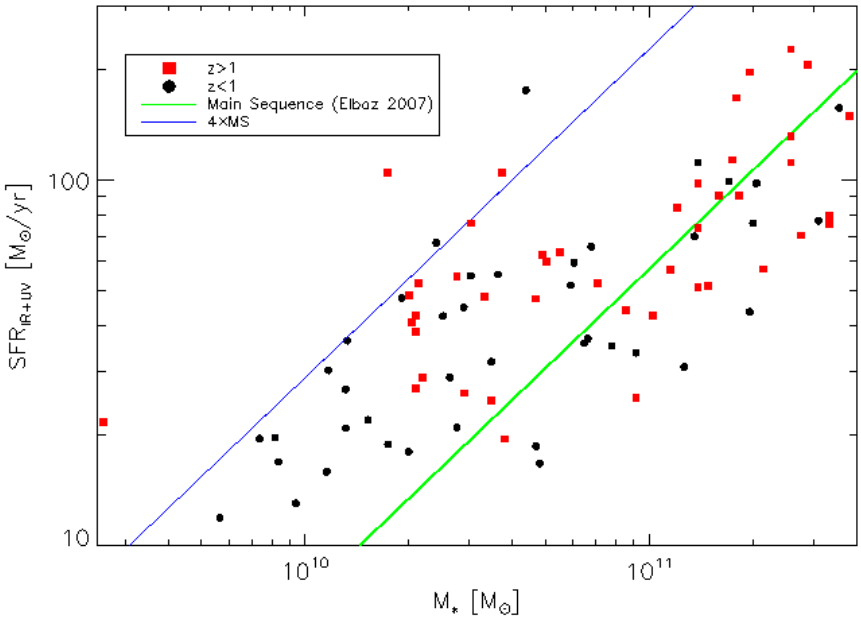

Figure 7.8: SFR_{IR+UV} versus M_*. The stellar masses are derived from the SED-fitting, the SFR are derived from the sum of the bolometric infrared luminosity ($\lambda \in [8-1000]\mu$) and the monochromatic UV luminosity at 2007 Å. The green solid line is the Main Sequence (MS) at redshift ~ 1 (Elbaz et al. 2007 [12]), the blue solid line is the 4×MS.
The filled red squares are the objects with redshift greater than one while the filled black circles are the sources with redshift lower than one. The sources with lower redshift show lower SFR's values while the high redshift objects are placed in the upper part of the Main Sequence.
The majority of the 3D-HST sources lie on the Main Sequence: only five galaxies are above the 4×MS and can be classified as outliers, as expected for a sample with strong Hα emission lines that needs to be intrinsically moderately obscured.

We report in Figure 7.9 how the MS is shaped when using the different SFR estimators analyzed in this Thesis. In this case we indicate with the black squares the measurements of SFR_{IR+UV}, while the red filled circles are the $SFR_{H\alpha}$ measurements derived using the color excess $E_{neb}(B-V)$, and computed with the conversion factor $f = \frac{E_{star}(B-V)}{E_{neb}(B-V)} = 0.69$ to correct for dust extinction.

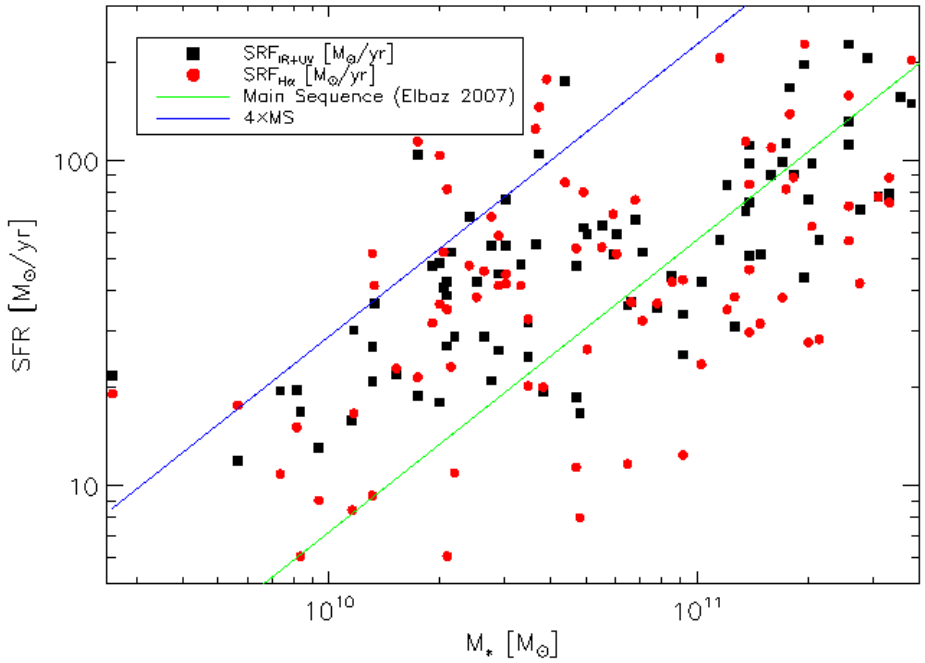

Figure 7.9: The plot shows the SFR versus M_*. The filled black squares indicate the values of SFR computed from the sum of L_{IR} and L_{UV}. The filled red circles represent the SFR derived from the $L_{H\alpha}$ corrected for dust extinction with the prescription of Kashino with an f-factor of $f = 0.69$, which gives the best estimate of dust extinction for our sample.

Table 7.1 lists the median values of attenuation $A_{H\alpha}$, the median values for the ratio $SFR_{IR+UV}/SFR_{H\alpha}$ and the rms of this ratio in respect to the 1:1 correlation line, by varying the adopted correction for dust extinction.

Dust correction	median $A_{H\alpha}$ [mag]	median $\frac{SFR_{IR+UV}}{SFR_{H\alpha}}$	$\sigma(\frac{SFR_{IR+UV}}{SFR_{H\alpha}})$
f=0.44	2.78	0.45	0.059
f=0.69	**1.78**	**1.15**	**0.016**
f=0.83	1.48	1.52	0.056
f=0.76	1.61	1.34	0.036
$A_{H\alpha} \propto M_*$	1.40	1.52	0.056
UV-slope β	1.55	1.48	0.052
$A_{H\alpha} \propto L_{IR}$	1.28	1.75	0.081

Table 7.1: Summarizing table which contains the median values of the attenuation on the Hα line, of the ratio $\frac{SFR_{IR+UV}}{SFR_{H\alpha}}$ and rms of the ratio $\frac{SFR_{IR+UV}}{SFR_{H\alpha}}$ in respect to the 1:1 line, by varying the dust extinction correction. The marked line highlights the dust correction method which leads to the best correlation between star formation rate indicators.

Chapter 8

Conclusions

In this Thesis we have analyzed the near-infrared spectra acquired from the slitless spectroscopic survey 3D-HST of a sample composed by 87 star-forming galaxies at redshift between 0.7 and 1.5.
The galaxies in the sample are an Herschel-PACS selection, so they are characterized by a strong infrared emission, produced mainly by a strong star formation activity. The objects were selected in the GOODS-S field throughout a cross correlation procedure in R.A. and Dec between the HST and the Herschel catalogs.
We considered in this selection only sources with a strong Hα emission line. We calculated the emission line fluxes and the spectroscopic redshifts for all the galaxies in the sample.
The SEDs were then fitted with the package MAGPHYS, using the photometry of the GOODS-MUSIC catalog, that spans the spectral range from U to far-IR. We have also correlated the MUSIC catalog with the photometry at 16μm so we used a total of 16 photometric bands for the SED fitting procedure.
We have then considered the problem of dust extinction, in order to apply a valid correction to our estimate of the Hα fluxes. Specifically speaking, we discussed about the relationship between the extinction on the stellar continuum $E_{star}(B-V)$ and the extinction on the nebular lines $E_{neb}(B-V)$.
We have taken into account especially four works:

- the Calzetti et al. (2000) [5] analysis on local galaxies
- the work of Kashino et al. (2013) [19] on star-forming objects at $z \in [1.4-1.47]$
- the Meurer et al. (1999) [33] study on the UV-slope of the spectrum on nearby starburst galaxies

- the Kennicutt et al. (2009) [22] approach on local sources

Each of these works suggests a different recipe to evaluate the extinction on the nebular lines. We applied the methodologies proposed by all these authors to correct the observed line flux and to obtain the intrinsic luminosity, from which we evaluate the $SFR_{H\alpha}$.
We calculated an independent estimate of the SFR from the sum of $L_{IR} + L_{UV}$.
To decide which is the more suitable method to estimate dust extinction in our sample, each of the $SFR_{H\alpha}$ estimates obtained by varying the dust extinction correction was compared with the SFR_{IR+UV}. Since we infer that intrinsically these indicators assume the same value, the mismatches between the two SFR estimates are produced mainly by the adopted dust extinction correction. Therefore the dust extinction correction that leads to the best correlation between SFR indicators was chosen as the best method for correcting our sample.
It results from our comparisons that the standard factor derived by Calzetti is too high since it yields to an overestimate of the $SFR_{H\alpha}$. The others estimates of dust correction lead to a better agreement between SFR indicators and the best trend was obtained using the relationship $E_{star}(B-V) = 0.69 \times E_{neb}(B-V)$ derived by Kashino et al. By adopting this extinction law we obtain a median attenuation $A_{H\alpha} \sim 1.78 mag$ that ranges between ~ 0.31 and ~ 4.05 magnitudes. The median $SFR_{H\alpha}$ for this extinction law results $\sim 42 M_{\odot}/yr$ with a range between $\sim 4 M_{\odot}/yr$ and $\sim 463 M_{\odot}/yr$, while the median SFR_{IR+UV} is $\sim 51 M_{\odot}/yr$ in a range $[12 - 482] M_{\odot}/yr$.
Our results are consistent with the last year literature, already cited in this Thesis (e.g. Wuyts et al. (2013), Price et al. (2013), Kashino et al. (2013), Ibar et al. (2013), Whitaker et al. (2014)).

As suggested by some authors, the presence and the value of differential extinction have a geometrical origin.
The dust model proposed to explain this behavior is a two component model which assumes the presence of a diffuse component of dust, that attenuates the light coming from all the stars, and a optically thick localized component (the *birth cloud*) that attenuates only the light of the most massive stars, which are able to ionize the surrounding medium and produce the Hα emission. If the number of these massive stars is higher, they will dominate the UV-visible continuum of the galaxy and also produce a strong Hα emission. Since these massive stars are located in the birth cloud (their lifetimes are too small to diffuse in the medium) the result is that the line attenuation will be comparable to the continuum attenuation.

Instead, if the galaxy hosts only few massive stars, then the continuum in the UV-visible is dominated by the less massive stars that are located in the diffuse ISM. The result in this case is that the line flux (produced again by the ionizing most massive stars) is more attenuated than the continuum light.
The conversion factor f is higher in the high redshift universe, in the past the attenuation on nebular lines is comparable to the attenuation on the continuum and so the most massive stars in distant galaxies are more uniformly distributed inside these systems.

The successive purpose of this work is to obtain an independent estimate of dust extinction on our 3D-HST sample. In order to compute this estimate we need a direct tracer of dust extinction, as the Balmer Decrement. In this sense we need to restrict the analysis on a more redshift-limited sample, considering the G141 grism features, which allow to detect the Hα line only in a range $z \in [0.7 - 1.5]$ and the Hβ line at $z \gtrsim 1.3$. Another way to estimate the correction for dust extinction for our sample is from the ratio between SFR_{far-IR} and $SFR_{far-IR+H\alpha}$ as proposed by Ibar et al. and already discussed in section 7.1.
It will be also opportune to eventually improve the reduction processes and to enlarge the sample, extending the analysis to the other fields observed in the 3D-HST survey.
Another purpose is to extend the photometric coverage of our PACS objects both at shorter wavelengths (correlating with GALEX data, for example) and longer wavelengths (PACS and SPIRE data) to improve our SED fitting procedure and the dust extinction estimate. Especially important in fact is to enlarge the coverage in the UV-rest frame spectrum to compute the UV slope from the photometry, so independently by the SED model. Having a greater quantity of data in the far-IR is useful to have a better estimate of dust luminosities and dust masses.
Finally it is our intention also to apply the same analysis discussed in this Thesis to the data of the spectroscopic survey FMOS/Subaru in the COSMOS field (P.I. Silverman, Silverman et al. (2014) [44]). The Fiber Multi-Object Spectrograph (*FMOS*) is a near-infrared spectrograph that uses fibers with 1.2 *arcsec* of diameter to simultaneously acquire spectra for about 200 galaxies over a circular region of $30'$ in diameter and has a spectral resolution in high-resolution mode of $\lambda/\Delta\lambda \approx 2600$ in the H-band. Four high-resolution gratings are designed to provide contiguous spectral coverage to cover the full J and H bands.
The FMOS survey is specifically designed to detect the Hα emission line from a sample of around one thousand star-forming galaxies with $M_* \leq 10^{10} M_\odot$ and $1.4 < z < 1.7$. The high-resolution mode of the spec-

trograph allows to separate Hα and [NII] emission lines thus enabling studies of gas-phase metallicity and photoionization conditions of the interstellar medium. Galaxies with Hα detections are followed up with FMOS observations at shorter wavelength to detect Hβ and $[OIII]_{\lambda 5007}$ that provides an assessment of extinction and an indication of embedded AGNs.

Acknowledgments

This work is based on observations taken by the 3D-HST Treasury Program (GO 12177 and 12328) with the NASA/ESA HST, which is operated by the Association of Universities for Research in Astronomy, Inc., under NASA contract NAS5-26555.
This work is also based on observations made with the NASA/ESA Hubble Space Telescope, and obtained from the Hubble Legacy Archive, which is a collaboration between the Space Telescope Science Institute (STScI/NASA), the Space Telescope European Coordinating Facility (ST-ECF/ESA) and the Canadian Astronomy Data Center (CADC/NRC/CSA).
We would like to thank Antonio Cava for the improvement to the IDL routine ***extract_grism_spec.pro***. We also thank Emanuele Daddi and Alvio Renzini for the useful discussions about the spectroscopical analysis and about the study on dust extinction.

List of Figures

List of Tables

List of Acronyms

ACS Advanced Camera for Surveys
AEGIS All-wavelength Extended Groth Strip International Survey
AGB Asymptotic Giant Branch
AGN Active Galactic Nucleus
CDM Cold Dark Matter
ESA European Space Agency
ESO European Southern Observatories
EW Equivalent Width
FMOS Fiber Multi-Object Spectrograph
GAIA Gra-phical Astronomy and Image Analysis Tool
GALEX GALaxy Evolution eXplorer
GOODS Great Observatories Origins Deep Survey
GOODS-MUSIC GOODS-MUltiwavelength Southern Infrared Catalog
GRASIL GRAphite and SILicate
HIFI Heterodyne Instrument for the Far Infrared
HST Hubble Space Telescope
IMF Initial Mass Function
IR Infra Red
IRAC Infra Red Array Camera
IRAF Image Reduction and Analysis Facility
IRS InfraRed Spectrograph
ISM InterStellar Medium
MAGPHYS Multi-wavelength Analysis of Galaxy PHYSical properties
MC Molecular Clouds
MIPS Multiband Imager Photometer for Spitzer
PACS Photodetector Array Camera and Spectrometer
PAH Polycyclic Aromatic Hydrocarbon
PEP PACS Evolutionary Probe
QSO Quasi Stellar Object
RT Radiative Transport
SED Spectral Energy Distribution
SFR Star Formation Rate

SPH Smoothed Particle Hydrodynamics
SPIRE Spectral and Photometric Imaging REceiver
SSP Simple Stellar Population
ULIRG Ultra Luminous InfraRed Galaxy
UV Ultra-Violet
UDS Ultra Deep Survey
WFC3 Wide-Field Camera 3
VIMOS VIsible MultiObject Spectrograph
VLT Very Large Telescope

Bibliography

[1] S. Berta, B. Magnelli, D. Lutz, et al. Dissecting the cosmic infra-red background with Herschel/PEP. *A & A*, 518:L30, July 2010.

[2] E. Bertin and S. Arnouts. SExtractor: Software for source extraction. *A & A*, 117:393–404, June 1996.

[3] G.B. Brammer, P. G. van Dokkum, M. Franx, et al. 3D-HST: A Wide-field Grism Spectroscopic Survey with the Hubble Space Telescope. *ApJs*, 200:13, 2012.

[4] G. Bruzual and S. Charlot. Stellar population synthesis at the resolution of 2003. *MNRAS*, 344:1000–1028, October 2003.

[5] D. Calzetti. The effects of dust on the spectral energy distribution of star-forming galaxies. *NewAR*, 45:601–607, October 2001.

[6] G. Chabrier. Galactic Stellar and Substellar Initial Mass Function. *PASP*, 115:763–795, July 2003.

[7] S. Charlot and S. M. Fall. A Simple Model for the Absorption of Starlight by Dust in Galaxies. *ApJ*, 539:718–731, August 2000.

[8] E. da Cunha, S. Charlot, and D. Elbaz. A simple model to interpret the ultraviolet, optical and infrared emission from galaxies. *MNRAS*, 388:1595–1617, August 2008.

[9] E. Daddi, M. Dickinson, G. Morrison, et al. Multiwavelength Study of Massive Galaxies at z˜2. I. Star Formation and Galaxy Growth. *ApJ*, 670:156–172, November 2007.

[10] T. de Graauw, F. P. Helmich, T. G. Phillips, et al. The Herschel-Heterodyne Instrument for the Far-Infrared (HIFI). *A & A*, 518:L6, July 2010.

[11] E. Diolaiti, O. Bendinelli, D. Bonaccini, L. M. Close, D. G. Currie, and G. Parmeggiani. StarFinder: A code for stellar field analysis, November 2000. Astrophysics Source Code Library.

[12] D. Elbaz, E. Daddi, D. Le Borgne, et al. The reversal of the star formation-density relation in the distant universe. *A&A*, 468:33–48, June 2007.

[13] D. K. Erb, C. C. Steidel, A. E. Shapley, et al. Hα Observations of a Large Sample of Galaxies at z ˜ 2: Implications for Star Formation in High-Redshift Galaxies. *ApJ*, 647:128–139, August 2006.

[14] N. M. Förster Schreiber, R. Genzel, N. Bouché, et al. The SINS Survey: SINFONI Integral Field Spectroscopy of z ˜ 2 Star-forming Galaxies. *ApJ*, 706:1364–1428, December 2009.

[15] A. Grazian, A. Fontana, C. de Santis, et al. The GOODS-MUSIC sample: a multicolour catalog of near-IR selected galaxies in the GOODS-South field. *A & A*, 449:951–968, April 2006.

[16] M. Griffin, P. Ade, P. André, et al. The SPIRE Instrument. In L. Pagani and M. Gerin, editors, *EAS Publications Series*, volume 34 of *EAS Publications Series*, pages 33–42, 2009.

[17] N. A. Grogin, D. D. Kocevski, S. M. Faber, et al. CANDELS: The Cosmic Assembly Near-infrared Deep Extragalactic Legacy Survey. *ApJs*, 197:35, December 2011.

[18] E. Ibar, D. Sobral, P. N. Best, et al. Herschel reveals the obscured star formation in HiZELS Hα emitters at z = 1.47. *MNRAS*, 434:3218–3235, October 2013.

[19] D. Kashino, J. D. Silverman, G. Rodighiero, et al. The FMOS-COSMOS Survey of Star-forming Galaxies at z ˜ 1.6. I. Hα-based Star Formation Rates and Dust Extinction. , 777:L8, November 2013.

[20] R. C. Kennicutt, Jr. Star Formation in Galaxies Along the Hubble Sequence. *ARAA*, 36:189–232, 1998.

[21] R. C. Kennicutt, Jr. The Global Schmidt Law in Star-forming Galaxies. *ApJ*, 498:541–552, May 1998.

[22] R. C. Kennicutt, Jr., C.-N. Hao, D. Calzetti, et al. Dust-corrected Star Formation Rates of Galaxies. I. Combinations of Hα and Infrared Tracers. *ApJ*, 703:1672–1695, October 2009.

[23] R. C. Kennicutt, Jr., P. Tamblyn, and C. E. Congdon. Past and future star formation in disk galaxies. , 435:22–36, November 1994.

[24] A. M. Koekemoer, S. M. Faber, H. C. Ferguson, et al. CANDELS: The Cosmic Assembly Near-infrared Deep Extragalactic Legacy Sur-

veyThe Hubble Space Telescope Observations, Imaging Data Products, and Mosaics. *ApJs*, 197:36, December 2011.

[25] X. Kong, S. Charlot, J. Brinchmann, and S. M. Fall. Star formation history and dust content of galaxies drawn from ultraviolet surveys. *MNRAS*, 349:769–778, April 2004.

[26] M. Kümmel, J. R. Walsh, N. Pirzkal, H. Kuntschner, and A. Pasquali. The Slitless Spectroscopy Data Extraction Software. *PASP*, 121:59–72, January 2009.

[27] C. Leitherer and T. M. Heckman. Synthetic properties of starburst galaxies. *ApJs*, 96:9–38, January 1995.

[28] B. Lo Faro, A. Franceschini, M. Vaccari, et al. The Complex Physics of Dusty Star-forming Galaxies at High Redshifts as Revealed by Herschel and Spitzer. *ApJ*, 762:108, January 2013.

[29] D. Lutz, A. Poglitsch, B. Altieri, et al. PACS Evolutionary Probe (PEP) - A Herschel key program. *A & A*, 532:A90, August 2011.

[30] P. Madau and M. Dickinson. Cosmic Star Formation History. *ArXiv e-prints*, February 2014.

[31] P. Madau, L. Pozzetti, and M. Dickinson. The Star Formation History of Field Galaxies. *ApJ*, 498:106–116, May 1998.

[32] B. Magnelli, D. Elbaz, R. R. Chary, et al. The 0.4 z 1.3 star formation history of the Universe as viewed in the far-infrared. *A & A*, 496:57–75, March 2009.

[33] G. R. Meurer, T. M. Heckman, and D. Calzetti. Dust Absorption and the Ultraviolet Luminosity Density at z ˜ 3 as Calibrated by Local Starburst Galaxies. *ApJ*, 521:64–80, August 1999.

[34] Y.-j. Peng, S. J. Lilly, K. Kovač, et al. Mass and Environment as Drivers of Galaxy Evolution in SDSS and zCOSMOS and the Origin of the Schechter Function. *ApJ*, 721:193–221, September 2010.

[35] G. L. Pilbratt, J. R. Riedinger, T. Passvogel, G. Crone, D. Doyle, U. Gageur, A. M. Heras, C. Jewell, L. Metcalfe, S. Ott, and M. Schmidt. Herschel Space Observatory. An ESA facility for far-infrared and submillimetre astronomy. *A & A*, 518:L1, July 2010.

[36] A. Poglitsch and B. Altieri. The PACS Instrument. In L. Pagani and M. Gerin, editors, *EAS Publications Series*, volume 34 of *EAS Publications Series*, pages 43–62, 2009.

[37] S. H. Price, M. Kriek, G. B. Brammer, et al. Direct Measurements of Dust Attenuation in z ˜ 1.5 Star-forming Galaxies from 3D-HST: Implications for Dust Geometry and Star Formation Rates. *ApJ*, 788:86, June 2014.

[38] N. A. Reddy, D. K. Erb, M. Pettini, et al. Dust Obscuration and Metallicity at High Redshift: New Inferences from UV, Hα, and 8 μm Observations of z ˜ 2 Star-forming Galaxies. *ApJ*, 712:1070–1091, April 2010.

[39] G. Rodighiero, A. Cimatti, C. Gruppioni, et al. The first Herschel view of the mass-SFR link in high-z galaxies. *A&A*, 518:L25, July 2010.

[40] G. Rodighiero, A. Renzini, E. Daddi, et al. A multiwavelength consensus on the main sequence of star-forming galaxies at z

2. *MNRAS*, 443:19–30, September 2014.

[41] E. E. Salpeter. The Luminosity Function and Stellar Evolution. *ApJ*, 121:161, January 1955.

[42] P. Santini, A. Fontana, A. Grazian, et al. GOODS-MUSIC catalog updated version (Santini+, 2009). *VizieR Online Data Catalog*, 350:40751, June 2009.

[43] K. B. Schmidt, H.-W. Rix, E. da Cunha, et al. The spatial extent and distribution of star formation in 3D-HST mergers at z

1.5. *MNRAS*, 432:285–300, June 2013.

[44] J. D. Silverman, D. Kashino, N. Arimoto, et al. The FMOS-COSMOS survey of star-forming galaxies at z˜1.6 III. Survey design, performance, and sample characteristics. *ArXiv e-prints*, September 2014.

[45] R. E. Skelton, K. E. Whitaker, I. G. Momcheva, et al. 3D-HST WFC3-selected Photometric Catalogs in the Five CANDELS/3D-HST Fields: Photometry, Photometric Redshifts and Stellar Masses. *ArXiv e-prints*, March 2014.

[46] H. I. Teplitz, V. Charmandaris, R. Chary, et al. 16 μm Imaging around the Hubble Deep Field-North with the Spitzer IRS. *ApJ*, 634:128–136, November 2005.

[47] K. E. Whitaker, M. Franx, J. Leja, et al. Constraining the Low-Mass Slope of the Star Formation Sequence at $0.5 < z < 2.5$. *ArXiv e-prints*, July 2014.

[48] S. Wuyts, N. M. Förster Schreiber, E. J. Nelson, et al. A CANDELS-3D-HST synergy: Resolved Star Formation Patterns at 0.7 z 1.5. *ApJ*, 779:135, December 2013.

[49] T. Yoshikawa, M. Akiyama, M. Kajisawa, et al. MOIRCS Deep Survey. VI. Near-infrared Spectroscopy of K-Selected Star-forming Galaxies at z ˜ 2. *ApJ*, 718:112–132, July 2010.